Holohan, E., Schöpfer, M. P. J., Walsh, J. J. (2015): Stress evolution during caldera collapse. - *Earth and Planetary Science Letters*, *421*, p. 139-151.

DOI: http://doi.org/10.1016/j.epsl.2015.03.003

Stress evolution during caldera collapse

E.P. Holohan[1,2], M.P.J. Schöpfer[1,3], & J.J. Walsh[1]

[1] GFZ Potsdam, Section 2.1 – Physics of Earthquakes and Volcanoes, Telegrafenberg, Potsdam 14473, Germany.

[2] Fault Analysis Group, UCD School of Geological Sciences, Dublin 4, Ireland.

(3) Department for Geodynamics and Sedimentology, University of Vienna, Althanstrasse 14, Vienna, Austria.

Email: holohan@gfz-potsdam.de

Abstract

The dynamics of caldera collapse are subject of long-running debate. Particular uncertainties concern how stresses around a magma reservoir relate to fracturing as the reservoir roof collapses, and how roof collapse in turn impacts upon the reservoir. We used two-dimensional Distinct Element Method models to characterise the evolution of stress around a depleting sub-surface magma body during gravity-driven collapse of its roof. These models illustrate how principal stress directions rotate during progressive deformation so that roof fracturing transitions from initial reverse faulting to later normal faulting. They also reveal four end-member stress paths to fracture, each corresponding to a particular location within the roof. Analysis of these paths indicates that fractures associated with ultimate roof failure initiate in compression (i.e. as shear fractures). We also report on how mechanical and geometric conditions in the roof affect pre-failure unloading and post-failure reloading of the reservoir. In particular, the models show how residual friction within a failed roof could, without friction reduction mechanisms or fluid-derived counter-effects, inhibit a return to the initial pre-collapse pressure in the magma reservoir. Many of these findings should be

transferable to other gravity-driven collapse processes, such as sinkhole formation, mine collapse and subsidence above hydrocarbon reservoirs.

Keywords: collapse calderas; subsidence; stress; ring-faults; stress paths; Distinct Element Method models.

1. Introduction

Extraction of material from a sub-surface body commonly causes the overburden to subside or collapse. Perhaps the most extreme instances occur with drainage of a sub-surface magma body. This can cause subsidence of many 100's or 1000's of metres within a few weeks or days (Geshi et al., 2002; Michon et al., 2007; Wilson and Hildreth, 1997), to form enclosed topographic depressions called pit-craters (diameter < 1 km) or calderas (diameter 1 – 100 km). A similar, smaller-scale natural phenomenon is sink-hole formation induced by karst-rock dissolution (Gutierrez et al., 2008). Man-made phenomena include ground subsidence or collapse induced by sub-surface mining (Walters, 1978; Whittaker and Reddish, 1989), water extraction (Arkin and Gilat, 2000) or hydrocarbon recovery (Nagel, 2001; Odonne et al., 1999). In all cases, removal of material from the sub-surface body causes deformation and stress changes within the surrounding host-rock. The host-rock eventually fails through to the surface, with often dramatic and adverse consequences for buildings, equipment, infrastructure and human safety. Characterisation of the host-rock stress field during depletion or extraction of material from below the Earth's surface is hence of multidisciplinary interest.

The dynamic (i.e. stress-related) attributes of caldera collapse, which are the focus of this paper, have been subject of a long-running debate. Several unresolved questions include:

(1) How does the stress field arising from magma reservoir depletion evolve with progressive deformation and fracturing during the reservoir roof's collapse?

(2) What are the modes of fracturing in the host rock around the reservoir and which of these is associated with ultimate roof failure?

(3) How are the evolutions of stress and fracturing in the reservoir roof coupled to pressure conditions in the reservoir?

Answers to these questions inform the theoretical framework for interpretation of geodetic, seismic and other geophysical data collected before, during and after a collapse event (Ekstrom, 1994; Fichtner and Tkalcic, 2010; Massin et al., 2011; Michon et al., 2011; Shuler et al., 2013). They are hence important for deformation monitoring and hazard assessment at not only volcanoes, but also to other natural or man-made instances of depletion-induced subsidence (Cesca et al., 2011; Dahm et al., 2011; Lenhardt and Pascher, 1996; Segall, 1989).

For caldera collapse, these answers are clouded by differing observations or interpretations of primary field or geophysical data, as well as by inconsistency of past modelling approaches or results. For example, some past analytical or numerical studies of stresses arising from reservoir depletion conclude that initial roof failure should occur along a reverse fault inclined outward from the reservoir centre (Anderson, 1936; Holohan et al., 2013; Sanford, 1959) (**Figure 1A**), whereas others conclude or assume that it should occur along a normal fault inclined toward the reservoir centre (Gudmundsson, 1998; Gudmundsson et al., 1997; Robson and Barr, 1964) (**Figure 1B**). This discrepancy arises in part because continuum-based analytic

cal and numerical approaches cannot simulate the large discontinuous (i.e. fault-related) strains characteristic of caldera collapse. Analogue models (Marti et al., 1994; Roche et al., 2000) or Distinct Element Method (DEM) numerical models (Hardy, 2008; Holohan et al., 2011) of caldera collapse can do so and produce both fault orientations (**Figure 1C**). Although these models are consistent with field and geophysical evidence from some well-exposed or well-monitored calderas (Clough et al., 1909; Fichtner and Tkalcic, 2010; Geshi et al., 2002; Holohan et al., 2009; Massin et al., 2011) (**Figure 1D**), they have not yielded information on how fracturing relates to stress. One consequence is an interpretative inconsistency in the literature about how the orientations of principal stresses and caldera faults relate to each other, e.g. (Roche et al., 2000) vs. (Lavallee et al., 2004) vs. (Michon et al., 2009).

Here we characterise the evolution of stress around a depleting sub-surface body from onset of roof subsidence through to the roof's failure and collapse. We do so with two-dimensional DEM models (Cundall and Strack, 1979) in which rock is represented by an assemblage of bonded particles (Potyondy and Cundall, 2004). The relatively-new DEM approach readily simulates the formation and growth of large-displacement fracture systems, and so can reveal their relationship to evolving stress-states. Moreover, our model formulation is such that roof stresses and fracturing are coupled to the reservoir's loading-unloading history. This enables relationships between roof fracturing, reservoir depletion and reservoir 'under-pressure' to be ascertained throughout the course of roof subsidence. While the model results primarily pertain to stress evolution during collapse into a depleting magma body, many of them should be transferable to other extraction-induced subsidence scenarios.

2. Numerical Methods and Model Set-Up

Our starting point for modelling caldera collapse is the following geological scenario. A dyke intrusion has begun to laterally drain a magma reservoir (e.g. (Geshi et al., 2002; Hildreth and Fierstein, 2000; Michon et al., 2007)). Pressure in the reservoir has returned to a 'lithostatically-equilibriated' value as the dyke's propagation and the onset of any associated eruption expended any related 'over-pressure' (Druitt and Sparks, 1984; Roche and Druitt, 2001). (Note: "lithostatic" or "magmastatic" here describe the origins of stress or pressure, as derived from the weight of overlying rock or magma, respectively. 'Lithostatically-equilibrated' thus refers to a reservoir pressure equal to that expected from the combined lithostatic and magmastatic loads.) Thereafter, magma withdrawal continues through the open dyke, even as the reservoir becomes 'under-pressured' relative to its lithostatically-equilibriated state and the roof eventually collapses without any eruption through it. Detailed observations of recent collapses at several volcanoes (Geshi et al.,

2002; Michon et al., 2007; Sigmundsson et al., 2015; Staudacher et al., 2009) support this scenario's plausibility.

We address this scenario numerically by using the two-dimensional DEM software PFC2D (Itacsa Consulting Group Inc., 2004). This simulates the motion of rigid disk-like particles that interact with each other and with rigid boundary walls according to simple elastic-frictional contact laws. Particles can be connected by beam-like elastic bonds that act in parallel with a linear contact law ('parallel bonds' - see (Potyondy and Cundall, 2004)). These bonds transmit both forces and moment between particles, and so enable elastic continuum behaviour at larger scale. Bonds break once their shear or tensile strength is exceeded. This ultimately causes path-dependent fracture development and failure of the DEM material (i.e. non-elastic discontinuum behaviour).

As in those of Holohan et al., (2011), our models comprised a 3 x 4 km assemblage of ca. 50,000 rigid, cylindrical (disk-like) particles that were randomly placed inside rigid, frictionless, boundary walls (**Figure 2**). Particle radii were uniformly distributed between 6 m and 10 m. Particle density was 2700 kgm^{-3}. Tests show that the main results shown below are essentially unaffected by changing the assemblage's boundary conditions, size or resolution (see **Supplementary Material**). The particles were first settled under gravity with a low friction coefficient of 0.01, and then grouped into one of two domains: 'host rock' or 'reservoir'.

Host rock particles were bonded and given a higher friction coefficient of 0.5. Varying the 'host rock' particle and bond properties produces a range of bulk properties (**Table 1**). These are characteristic of natural volcanic rock masses, and were estimated from simulated biaxial tension and compression tests (for further details and discussion see (Holohan et al., 2011)). For illustration purposes, a Hoek-Brown failure envelope for the host rock was fitted to the maximum stress states attained within a model-wide array of overlapping measurement circles of 75 m radius. Mechanical properties varied here included the host-rock's unconfined compressive (UCS) and tensile (UTS)

strengths and its Young's modulus (E) (**Table 1**). We also varied a key geometric property, namely the reservoir roof's thickness/diameter (T/D) ratio.

Reservoir particles were grouped to form a c. 1,200 x 300 m (i.e., sill-like) body, and left in the un-bonded, low friction state. Notwithstanding shear stresses arising within the reservoir and on the reservoir/host-rock boundary, related to particle interlocking (see **Supplementary Material**), these simple conditions enabled a fluid-like behaviour (particulate flow) and related stress redistribution in the reservoir. They also provided numerical stability for large strains of the reservoir/host-rock boundary. Further reducing the particle friction coefficient has no notable effect on either the reservoir or host-rock behaviour (see **Supplementary Material**). An alternative 'super-bonded' reservoir-host rock boundary condition was also tested. This produces quite similar results at low (elastic strains), and also for the general evolution of fracturing in the host rock, but leads to rather unrealistic reservoir behaviour at high depletions (see **Supplementary Material**).

For simplicity, we assume that reservoir depletion occurs at a constant rate, which was simulated by a slow, constant, incremental reduction of each reservoir particle's area, up to a value of 50%. This slow depletion, combined with damping of particle accelerations, ensured quasi-static model behaviour. Dyke propagation and magma outflow attending depletion were assumed to occur in a direction perpendicular to the 2D plane of cross-section in the model, and hence they were not directly simulated. Both reservoir and host-rock could deform freely in reaction to the gravitational loading during depletion.

Stress and strain, which are continuum quantities, were computed at 1% depletion intervals through averaging procedures (Potyondy and Cundall, 2004). In the host-rock, the maximum finite shear strain was chosen as a measure of strain localisation and was calculated from displacements within a radius of 25 m around each particle, which was then coloured accordingly. Principal stress magnitudes, as well as differential stress magnitudes, were visualised by colouring each particle

146 according to the sum of the particle contact forces divided by the particle area (see Eq. 52 in
147 (Potyondy and Cundall, 2004)). Principal stress orientations were on the other hand plotted after
148 first averaging particle stresses and interpolating them upon a 125 x 125 m grid. Stress paths were
149 constructed for selected areas of interest from the average particle stress tensor within a circular
150 area of radius 75 m (see Eq. 57 in (Potyondy and Cundall, 2004)). In the reservoir, pressure was
151 defined as the mean stress within a circular area of radius 75 m that was located in the bottom half
152 of the reservoir domain.

153 The geometric and mechanical properties of the models shown below are most applicable to
154 small-scale caldera collapses (Geshi et al., 2002; Michon et al., 2007). Given an apparent scale-
155 independence of the main features of caldera structure (Branney, 1995), however, much of the
156 dynamic model behaviour is likely transferable to larger-scale. Additional factors potentially
157 affecting caldera collapse in nature, such as stresses from regional tectonics (Gudmundsson et al
158 1997), topographic loads (Pinel 2011) or three-dimensional geometric effects (Roche and Druitt
159 2001, Holohan et al., 2008, 2013) were not examined here, but could be a subject of future work.

160 ## 3. Results

161 **Figure 3** schematically summarises the structural styles of collapse seen in DEM caldera
162 collapse models as the reservoir roof's geometric and mechanical properties are varied (see
163 (Holohan et al., 2011) for details). The most typical style formed within the investigated parameter
164 space is the 'single central block' collapse style; the others in this figure develop at the geometrical
165 and mechanical extremes. Consequently, we focus below on the stress evolution in a representative
166 'single central block' collapse style. The main features of this stress evolution occur in all of the
167 other collapse styles also, however **(see Supplementary Material**).

3.1 Depletion-induced stress patterns and host-rock fracturing

A key advantage of the DEM approach is the ability to directly compare the strain and stress evolutions of the simulated caldera collapse as they emerge and interrelate during progressive deformation. **Figure 4** hence shows strain localisation, stress orientation and stress magnitude at several stages of the representative model's evolution.

Prior to depletion (**Figure 4, first row**), maximum compressive principal stress (σ_1) orientations are predominantly steeply inclined or vertical as a consequence of gravity. Deviations arise locally where significant non-vertical inter-particle contact forces occur within an averaging region. These reflect the anastomosing inter-particle force chains in the assemblage.

The 'host rock' deforms elastically during the earliest increments of reservoir depletion (**Figure 4, second row**). A general inward movement of the host rock toward the reservoir causes σ_1 orientations to wrap around the reservoir and so define a 'stress arch' above it and a 'stress bowl' below it. Relative to initial lithostatic values, σ_1 magnitudes increase in the upper central and lower marginal parts of the reservoir roof, but they decrease both in the lower central part of the roof and in the central part of the floor. Magnitudes of the minimum principal stress (σ_3) generally decrease in the roof and in the floor, except at the tips of the sill. In two peripheral areas lying near the model surface, σ_3 magnitudes decrease to negative (i.e. tensile) values. Significantly, the combination of decreased σ_3 and increased σ_1 magnitudes results in relatively large differential or shear stresses in the roof's upper central and lower marginal parts. The distribution of the high differential stresses also follows an arch-like pattern in the roof (cf. (Folch and Marti, 2004; Holohan et al., 2013)).

With increased reservoir depletion, the 'host rock' begins to deform non-elastically (**Figure 4, third row)**. Damage (broken bonds) accumulates, significant fractures develop and eventually the

191 reservoir roof fails. The main fractures formed at this stage typically include near-vertical fissures
192 and outward-dipping (reverse) faults. The fissures relax the tensile stress developed in the
193 peripheral near-surface areas. The outward-dipping faults pass through the roof's lower marginal
194 and upper central parts, where their development locally decreases the σ_1 magnitudes. Conversely,
195 differential stresses increase in the roof's upper marginal parts - i.e., in the hanging walls of the
196 outward-dipping faults. Also, σ_1 orientations here undergo a subtle outward-rotation and
197 steepening. With still further reservoir depletion, additional outward-dipping faults may form as
198 splays from the initial ones. In a reflection of the steepening of σ_1 orientations, the newer faults dip
199 more steeply than the older faults.

200 At the latest stages of depletion, inward-dipping faults eventually develop in the areas
201 outward of the reservoir margin (**Figure 4, fourth row**). Their formation substantially relaxes the
202 recently increased σ_1 magnitudes and differential stresses there. Also, their inward dip reflects a
203 further outward rotation and steepening of the σ_1 directions to near-vertical. The lower tip of each
204 normal fault typically links with an outward-dipping fault or with the reservoir's lateral edge. The
205 upper tip usually links with an earlier-formed crack near the surface.

206 Overall, the process of fracturing and failure of the reservoir roof is associated with a
207 progressive disruption of the stress arch seen in the initial elastic phase. Nonetheless, a more
208 spatially-irregular stress arching persists within the collapsing roof even after formation of all the
209 main fractures.

210 ***3.2 Stress paths to host-rock fracturing***

211 Analysis of the paths taken through principal stress space toward fracture (cf. (Schopfer et al.,
212 2006)) gives further insights into the mode of failure of the reservoir roof. **Figure 5** shows such
213 paths for the main areas of fracture within the representative 'single central block collapse' model.

All paths in the host rock start close to a line with a slope of one, denoting initial lithostatic stress conditions that are close to isotropic (i.e., $\sigma_1 = \sigma_3$). This is because of the low inter-particle friction during initial settling. The exact starting point of each path is related to the initial depth of the analysed area of fracture; paths for deeper areas start at higher values of both principal stresses (i.e. toward the top and right of the diagram). As the reservoir is depleted, the principal stress states all move toward the host rock's failure envelope.

In the lower central part of the reservoir roof, the stress state moves along a downward path (red in **Figure 5**) that is almost parallel to the isotropic line. This indicates a progressive near-isotropic decrease in both σ_1 and σ_3 in this area immediately above the reservoir. In the roof's lower marginal parts (green and light blue paths in **Figure 5**) and in its upper marginal parts (pink path in **Figure 5**), the paths are orientated at c. 90° to the isotropic line. This shows that the areas where the major outward-dipping (reverse) and inward-dipping (normal) faults eventually form are characterised by an initial σ_1 increase coupled with a σ_3 decrease.

Near the model surface, the stress path in the roof's central part (black path in **Figure 5**) is orientated at c. 45° counter-clockwise to the isotropic line, showing that σ_1 increases while σ_3 remains unchanged. Conversely, the stress path in the roof's peripheral area (dark blue path in **Figure 5**) runs at c. 45° clockwise to the isotropic line, and so here σ_3 decreases while σ_1 remains unchanged. The stress evolutions in both of these near-surface areas are hence characterised by almost uniaxial, rather than biaxial, loading conditions.

After reaching the failure envelope, most stress states retreat toward the isotropic line. Detailed comparison of the strain and stress field evolutions in the model shows that such retreat is usually associated with initial fracture formation or with rupture (i.e. a slip event on an existing fracture – seen as relatively sudden increases in shear strain) within the related area of the roof. A

straightforward example is the stress state evolution in the vicinity of fracture T4. Sequential strain plots such as in **Figure 4** show that T4 forms between 17-18% depletion, an interval corresponding to a sudden retreat along the related stress path (dark blue path in **Figure 5).** A more complex example concerns the outward-dipping fractures, R1 and R2. Sequential strain plots show that R1 and R2 begin to form after 9% and 10 % depletion, but undergo major ruptures between 10-12% and 13-16% depletion, respectively. The sharpest retreat along each stress path (see the green and light blue paths in **Figure 5**) hence coincides with a rupture event, rather than initial fracture formation, in these cases (i.e. stress-drops are not instantaneous after failure).

Lastly, the stress path analysis reveals that most of the material fracture occurs in compression and thus that the overriding mode of roof failure is in shear. Only the near surface marginal fractures form in tension.

3.3. Reservoir unloading and reloading

The above-described stress and fracturing evolution within the model host-rock stems from a redistribution of gravitationally-induced stresses as the model reservoir is depleted. Since both the model reservoir and its host-rock are free to deform under gravity, these stresses can in principle be redistributed back onto the reservoir once the roof has failed. In this sense, the depletion-induced stress evolutions of the model host-rock and the reservoir are coupled.

Figure 6A shows the details of this host-rock/reservoir coupling in our representative model. It is important to note that the reservoir pressure here stems only from the weight of the reservoir particles themselves and the load exerted by the host-rock, since we neglect effects of magma incompressibility, volatile release, and eruption-related fluid dynamics. Changes in model reservoir pressure hence arise from the constant-rate reduction of mass within the reservoir (magmastatic

component) and, of greatest interest here, from any increase or decrease in the roof load acting on the reservoir (lithostatic component).

Effects of host-rock fracturing upon the reservoir pressure are highlighted by comparing the reservoir pressure evolution of the representative model with that of a geometrically-identical model in which fracturing of the host-rock was not permitted (**Figure 6A**). In the non-fractured model, the reservoir pressure first decreases rapidly then declines gently. The initial rapid decrease in pressure primarily represents an unloading of the reservoir that stems from the roof's ability to support its own weight elastically as material is withdrawn from under it. The subsequent gentler decline relates only to the continued reduction of the reservoir's mass beneath the non-fractured and entirely self-supported roof. This decline can hence be used to constrain the depletion-adjusted reservoir pressure that should be observed if the full load of the roof were re-established.

Unloading of the representative model reservoir during the initial elastic phase of host-rock strain (0-5% depletion) is seen as a rapid, near-linear decline in reservoir pressure that matches its non-fractured equivalent (**Figure 6A**). The onset of permanent strain in the form of bond breakage and associated minor fracturing in the host-rock is seen in a divergence from the 'non-fractured' pressure curve after about 5% depletion. At 7-9% depletion, the reservoir pressure in the representative model levels off and even kicks slightly upward. This mainly reflects the formation of near-surface fractures, particularly T1 and T2. Thereafter, however, the reservoir pressure decreases further and reaches a minimum at about 12% depletion. This marks the "ultimate strength" of the roof; further depletion results in the roof's "ultimate failure".

Reloading of the model reservoir following the roof's ultimate failure occurs episodically and in close association with the formation or slip of major fractures in the roof (**Figures 6A)**. A first sharp increase in reservoir pressure occurs between 12-16% depletion, shortly after or in conjunction with formation and rupture of the major fractures R1 and R2 (see also **Figure 4** and

283 related stress paths in **Figure 5**). Further phases of rapid pressure increase at 18-21% and 30-33%
284 are also related to later ruptures of R1 and R2, as well as to the formation of faults R3 and N1.

285 The unloading-reloading history is strongly affected by the roof's T/D ratio and the host-rock
286 Young's modulus (**Figure 6B**, **6C)**. Host-rock strength has a more subordinate influence (see
287 **Supplementary Material)**. Increasing Young's modulus increases the rapidity, in depletion terms,
288 of the initial unloading. Increasing T/D ratio increases the magnitude of reservoir unloading or
289 'under-pressure' that is sustained by the roof. Reloading of the reservoir is increasingly gradual
290 with increased T/D, and, even after all the main fractures have formed, is increasingly inhibited
291 from returning to depletion-adjusted lithostatic equilibrium.

292 ***3.4. Reservoir conditions at ultimate failure***

293 The minimum of the reservoir pressure vs. depletion curve corresponds to the critical condition for
294 the ultimate failure of the reservoir roof and the onset of roof collapse. **Figure 7** contains plots of
295 these critical conditions calculated over the investigated range of roof thicknesses and mechanical
296 properties.

297 Here one can see that the critical depletions and pressure drops increase with increased T/D. The
298 critical pressure drop is also subtly dependent on the roof's unconfined strength. For a given T/D
299 ratio, stronger roofs require larger pressure drops to fail (most notable in the normalised plots). This
300 effect seems most pronounced at lower T/D ratios. Any dependence of critical depletion on
301 unconfined strength is unclear from these data. For the same T/D, model roof's with high or low
302 Young's modulus fail at similar pressure drops (normalised or not). However, roofs with higher
303 Young's modulus fail at consistently smaller critical depletions.

4. Discussion

4.1. Outward- vs. inward-dipping caldera ring faults: a unified dynamical explanation

There has been a several-decade-old debate about the nature of fractures accommodating caldera collapse and how their formation relates to the stress field induced by a magma reservoir. This debate was sparked by observations that the dip of ring-faults or ring-dykes, the major subsidence-accommodating fractures in nature, appeared to vary from steeply outward (e.g. (Richey and Thomas, 1932) to vertical (e.g. (Billings, 1945)) to steeply inward (e.g. (Lipman, 1976)). In some cases, this variation was even reported to occur laterally around an individual ring fault system (e.g. (Clough et al., 1909)).

An early attempt to mechanically explain ring fault inclination was Anderson's ((Anderson, 1936)) seminal analytical study. By relating the arched orientations of principal stresses around a depleting magma body to those of *initial* fractures, Anderson's theory can account for the formation of outward-dipping (reverse) ring faults (**Figure 1A**). Inward-inclined (normal) ring faults are not accounted for, but are commonly reported in field studies (Lipman, 1984). This apparent discrepancy motivated other workers to find mechanical scenarios in which magma reservoir depletion could lead to *initial* fractures that were inward-dipping normal faults.

Indeed, many of subsequent numerical or analytical studies of caldera ring fault formation started from premises that effectively discount the formation of outward-dipping (reverse) faults (e.g. (Folch and Marti, 2004; Gudmundsson, 1998; Gudmundsson et al., 1997; Pinel, 2011; Pinel and Jaupart, 2005). In contrast to Anderson's ((Anderson, 1936)) theory, these studies exclusively or primarily considered stress magnitudes, rather than stress orientations. This school of thought has an important common feature: near-surface tensile failure above or within a certain lateral distance

of the reservoir margin is thought to mark the onset of inward-inclined ring faulting and of roof failure (**Figure 1B**).

The idea that the roof of a depleting magma reservoir initially fractures and subsides along an inward-dipping ring fault is geometrically problematic, however. This has been long referred to as the 'space problem' of caldera subsidence (Branney, 1995; Lipman, 1984). Analogue collapse experiments (e.g. (Marti et al., 1994; Roche et al., 2000)) have consistently indicated that inward-inclined normal ring-faults form *not as initial fractures,* but develop after the formation of outward-dipping reverse ring-faults (**Figure 1C)**. Moreover, the scarcity of reverse faults in the geological record is likely explained by a low preservation potential stemming from their more central position within the collapsing roof and their inherently unstable overhanging scarps (Branney, 1995). These insights accord very closely with the best observed caldera collapse in nature to date at Miyakejima in 2000 (**Figure 1D**).

By explicitly simulating fracture system development during caldera collapse, our DEM models may resolve this debate over the dynamic conditions leading to differing ring fault orientations. In agreement with Anderson's (1936) theory, and for most geometric and mechanical configurations, ultimate failure of the roof above an under-pressured magma reservoir occurs along steep outward-dipping reverse faults. The term 'ultimate failure' is important here. In many situations, typically with low T/D and high strength, significant near-surface tensile failures occur first, as predicted in the above-mentioned studies that focused on stress magnitudes. The DEM model reservoir pressure evolutions (**Figures 6, S10**) show, however, that such tensile failures do not directly result in the roof being unable to support its own weight. Near-surface tensile fracture is hence a superficial or 'cosmetic' failure mode. 'Ultimate failure' occurs with the formation of fractures that disrupt the principal stress arch and reduce the roof's ability for self-support. The stress-arching entails a component of horizontal compression and so, unless this relaxed by ductile

behaviour such as down-sagging (Branney 1995, Holohan et al., 2011) (**Figs. 3, S5**), the initial fractures formed at ultimate failure must be reverse faults that are most typically outward-inclined.

The DEM models further show that the mechanical conditions for the formation of inward-dipping (normal) faults arise only *after* the stress arch has been disrupted. Stress arch disruption, either through creep or fracture, leads to an increase of differential stress in the areas marginal to the reservoir where inward-dipping normal faults subsequently form. This is similar to the concept of Coulomb stress transfer that is used to explain how an initial faulting event influences the location of subsequent fault activity (Stein et al., 1994). Additionally, stress arch disruption causes a steepening of the maximum principal stress trajectories in the areas marginal to the reservoir, such that faults forming at an acute angle to these trajectories (Anderson, 1951) are inward-dipping and normal. Although surface tensile fracturing *does not* mark their formation, the inward-dipping normal faults typically link with such tensile fractures at a later stage.

4.2. Stress paths to fracture during caldera collapse: implications for the formation of ring dykes

Another novel finding from our models is that different parts of the roof above a depleting reservoir take distinctive stress paths toward fracturing (**Figure 5 & S9**). As shown in **Figure 8**, we identify four end-member stress paths.

Two of these end-member paths, occurring near the surface, are characterised by a change in one principal stress only. In the roof centre, σ_1 increases (at constant minimum stress – **Figure 8**), thereby pushing the stress state toward compressive failure and formation of a central pop-up structure (analogous to 'wrinkle ridges' found in many calderas on Mars – e.g. (Mouginis-Mark and Robinson, 1992). In the roof periphery, σ_3 decreases (at constant maximum stress – **Figure 8**), thus moving the stress state toward tensile failure and the formation of marginal fissures.

373 The other two end-member paths, occurring at depth, are characterised by changes in both
374 principal stresses. In the lower central part of the roof, the stress state moves along a path parallel to
375 the isotropic line (at constant differential stress – **Figure 8**). In the limit, this path might intersect
376 the failure envelope in the tensile field to form near-horizontal 'cross fractures', as seen in some of
377 our other DEM models (Holohan et al., 2011). In nature, such cross fractures could mark the upper
378 edge of a sub-surface cavity or of a ring-dyke 'cap' (cf. (Anderson, 1936)). In lower and upper
379 marginal parts of the roof, the stress state moves along a path perpendicular to the isotropic line (at
380 constant mean stress – **Figure 8**). This leads to failure in compression and the formation of the
381 major outward-inclined reverse faults or inward-inclined normal faults.

382 This analysis indicates that shear fracturing predominates over tensile fracturing in the
383 subsiding reservoir roof. Moreover, our results support Anderson's (Anderson, 1936) inference that
384 ring-dykes, the steeply-inclined or bell-shaped intrusions found at many eroded volcanoes and
385 thought to act as main conduits for caldera-forming eruptions, initiate as shear fractures (i.e. faults).
386 A caveat is that our models do not include the effects of host-rock pore-fluid pressures, which, if
387 very high, could in theory favour tensile failure. The (in)significance of pore-fluid pressures for
388 caldera collapse in nature is unknown, however. The prediction that ring-dykes form in shear is
389 nonetheless supported by brecciation or cataclasis of the host rock at some well-exposed ring-dyke
390 margins (e.g. (Clough et al., 1909; Holohan et al., 2009; Kokelaar, 2007)).

391 In addition to insights for fracture system development at calderas, such DEM-based stress
392 path analysis may serve as a guide for future modelling aimed at understanding the relationship of
393 in-situ stresses and induced seismicity related to subsidence at working mines (e.g. (Kinscher et al.,
394 2015)) or hydrocarbon fields (e.g. (Hettema et al., 2000; Odonne et al., 1999; Segall, 1989)).
395 Furthermore, this type of analysis is likely transferrable to the study of the mechanics of sinkhole
396 formation in karst regions (Gutierrez et al., 2008; Poppe et al., 2015). Despite differences in scale,

driving mechanisms (e.g. fluid body pressure reduction vs. pore-fluid pressure reduction vs. solid mass removal) and deformation timescales, these non-volcanic subsidence phenomena show many structural, geophysical and geodetic similarities with volcanic collapses. Such similarities presumably arise primarily from their common feature: gravitationally-driven subsidence or collapse of the overburden into a sub-surface zone of volume loss.

4.3. Coupling of reservoir and host rock stress evolutions during caldera collapse

Caldera collapse involves coupling between the dynamics of the magma body and the host rock. Most past modelling studies have investigated this coupling to the point of roof failure in order to examine the reservoir's response to depletion or to estimate reservoir depressurisation or depletion needed for the onset of collapse (e.g. (Folch and Marti, 2004; Roche and Druitt, 2001)). Investigations of this coupling beyond roof failure have mainly been concerned with the fluid dynamics of the reservoir and their effects on related seismicity (Kumagai et al., 2001; Stix and Kobayashi, 2008); Stix and Kobashi 2008), intrusion (Kennedy et al., 2008), or eruption (Folch and Marti, 2009). Such post-failure coupling studies have hence assumed a simplistic, typically-fixed fault structure within the roof, and have not considered the potential impacts of varying the host-rock's mechanical properties. Our DEM models overcome these limitations.

On the other hand, a physio-chemically complete simulation of the magma reservoir's behaviour is beyond the scope of this work. In particular, we neglect the strain rate-, temperature- and pressure-dependent complexities of magma fluid dynamics and rheology. We also neglect changes in magma extraction rate (e.g. (Staudacher et al., 2009)) that may relate to such complexities or to feedbacks with the roof's collapse. These fluid-dynamical effects can significantly influence a natural reservoir's exact pressurisation history with respect to depletion and roof collapse (Roche and Druitt, 2001). Consequently, we limit ourselves here to a semi-

quantitative examination of the host-rock's potential contributions to the reservoir's pressurisation history, in terms of the unloading and reloading of the reservoir by the roof.

The rapid initial decline in reservoir pressure with magma withdrawal in our models (**Figure 6a**) is very similar to that predicted in many previous studies (Druitt and Sparks, 1984; Folch and Marti, 2009). One previously-identified influence on this decline's rate is the reservoir's bulk modulus (i.e., it's (in-) compressibility), with higher modulus leading to a more rapid pressure decline (Druitt and Sparks, 1984; Kumagai et al., 2001; Stix and Kobayashi, 2008). Our models indicate that the host-rock Young's modulus plays a very similar role, whereby host-rocks of higher modulus enable a more rapid transfer of stress from the reservoir into the initially self-supporting roof (**Figure 6b,c**). A consequence is that higher modulus host rocks require lower critical depletion values to reach the critical stress for roof failure and hence to begin reloading the reservoir (**Figure 7a**). In combination with other factors, such as low magma compressibility or pre-existing ring faults, this effect of host rock modulus may in part explain why some critical depletion levels estimated in nature (Michon et al., 2011) are much less than those predicted by past analogue models (Geyer et al., 2006) or analytical studies (Roche and Druitt, 2001).

The critical reservoir pressure decrease, or unloading, prior to roof failure is most strongly influenced by the T/D ratio in our models (**Figure 6 and 7**). This is a conclusion of several previous studies (e.g. (Folch and Marti, 2004; Holohan et al., 2013), including some accounting more rigorously for the reservoir dynamics (e.g. (Roche and Druitt, 2001)). The main reason is that, as in nature, the host-rock's frictional or shear strength increases with increased confining pressure, i.e. with increased depth (see Fig. 4 in (Holohan et al., 2011)). Critical depletion therefore also increases with T/D (cf. (Geyer et al., 2006; Roche and Druitt, 2001)), but, as noted above, also depends on the moduli of both reservoir and host rock. This effect of T/D helps explain why large

443 eruptions from deep reservoirs may occur without resulting in collapse at surface (Lavallee et al.,
444 2006).

445 In addition, our DEM models show that the unconfined strength of the host-rock has only a
446 secondary influence on the critical reservoir pressure decrease, and it is most clearly expressed at
447 lower T/D ratios (i.e. at shallower depths). This is likely because, with greater depth, the
448 contribution of cohesion to the total rock strength is proportionally decreased relative to that of
449 friction.

450 Roof collapse in our models does not necessarily return the reservoir pressure to a
451 lithostatically-equilibriated value (**Figure 6**). This is in contrast to an assumption of many past
452 studies of caldera formation (e.g. (Druitt and Sparks, 1984; Folch and Marti, 2009; Legros et al.,
453 2000). A return to such a value is seen only in the lowest T/D (0.2) ratios tested. For higher T/D
454 ratios, our models show that post-failure reloading of the reservoir is inhibited by the residual
455 frictional strength within faulted reservoir roofs, which leads to a persistence of stress arching there
456 (**Figure 4**). Moreover, this effect is enhanced with increased roof T/D ratio (i.e. reservoir depth).
457 For hydrocarbon fields, such loading of a reservoir by its subsiding roof is a common and often
458 important factor for enhancing recovery via a so-called ‘compaction drive’ that acts to increase
459 reservoir pore fluid pressure (Nagel, 2001). Numerical and analytical studies of hydrocarbon
460 reservoir compaction indicate that such compaction drive is inhibited by an increased T/D ratio
461 (Addis et al., 1998; Alassi et al., 2006), a finding in line with our results here.

462 Given the limitations of our approach, we do not argue that magma reservoir pressures cannot
463 in reality reach or even exceed lithostatic values after the onset of caldera collapse. Rather, our
464 models indicate that additional factors are likely required to achieve this. These might include
465 sufficiently reducing the friction on faults by magma intrusion or frictional melting ((Kokelaar,

466 2007)), or else additionally increasing the pressure in the reservoir by exsolution of volatiles (Druitt
467 and Sparks, 1984), or a combination of such phenomena.

468 Nevertheless, an inhibition of reservoir reloading after its roof collapses may help to explain
469 why some caldera-forming eruptions do not obey past model predictions (Druitt and Sparks, 1984;
470 Folch and Marti, 2009) that magma discharge rates and volumes should be higher after the onset of
471 collapse than beforehand. During the 1912 Katmai eruption, for example, only about 20% by
472 volume of magma was erupted after the inferred onset of collapse and the discharge rate *decreased*
473 by an order of magnitude (Stix and Kobayashi, 2008). This observation and the high T/D value
474 inferred for Katmai (T/D > 2.0) (Stix and Kobayashi, 2008) are consistent with the depth-increasing
475 inhibition of reservoir reloading following roof collapse in our models.

476 ## 5. Conclusions

477 The main conclusions of this study, summarised schematically in **Figure 9,** are as follows:

478 1. The evolution of stress during caldera collapse begins with the formation of a stable 'stress arch'
479 in the roof of a depleting magma reservoir. Ultimate failure of the reservoir roof occurs when the
480 stress arch is disrupted by the formation of reverse faults that are typically outward-inclined.

481 2. Disruption of the stress arch results in stress transfer to the roof margins and outward rotation of
482 stress directions there, which in turn leads to the formation of inward-inclined normal faults.

483 3. Near-surface tensile fracturing is not necessarily indicative of ultimate roof failure or of ring fault
484 formation.

485 4. There are four end-member stress paths taken toward fracturing and roof failure during caldera
486 subsidence. Each end-member path characterizes a particular part of the reservoir roof.

5. The depleting magma reservoir is rapidly unloaded while the reservoir roof initially supports its own weight, an effect that is more pronounced with higher Young's modulus of the host-rock. In nature, this may affect crystallization and volatile exsolution within the magma reservoir.

6. Roof collapse acts to reload the magma reservoir, with fault ruptures possibly causing sharp increases in reservoir re-pressurization. Residual friction within the down-going roof acts to inhibit full reloading of the reservoir, however. This effect increases with increasing reservoir depth.

Acknowledgements

We thank the staff of the Itasca Consulting Group for PFC-2D licenses and technical support under an Itasca Education Partnership. We are also grateful to Julia Morgan and two anonymous reviewers for their thoughtful comments and suggestions for improving this paper. This research was funded by a Government of Ireland Postdoctoral Fellowship (2007-2009) to EPH from the Irish Research Council. An International Mobility Fellowship (2009-2012) to EPH and co-funded by the Irish Research Council and Marie-Curie Actions is also gratefully acknowledged.

References

Addis, M.A., Choi, X., Gunning, J., 1998. The Influence Of The Reservoir Stress-Depletion Response On The Lifetime Considerations Of Well Completion Design. Society of Petroleum Engineers.

Alassi, H.T.I., Li, L.M., Holt, R.M., 2006. Discrete element modeling of stress and strain evolution within and outside a depleting reservoir. Pure Appl Geophys 163, 1131-1151.

Anderson, E.M., 1936. The dynamics of the formation of cone-sheets, ring-dykes, and cauldron subsidences. Proceedings of the Royal Society of Edinburgh 56, 128–157.

Anderson, E.M., 1951. The dynamics of faulting and dyke formation with applications to Britain, 2nd ed. revised. ed. Oliver & Boyd.

Arkin, Y., Gilat, A., 2000. Dead Sea sinkholes - an ever-developing hazard. Environ Geol 39, 711-722.

512 Billings, M.P., 1945. Mechanics of igneous intrusion in New Hampshire. American Journal of
513 Science 243, 40-68.

514 Branney, M.J., 1995. Downsag and Extension at Calderas - New Perspectives on Collapse
515 Geometries from Ice-Melt, Mining, and Volcanic Subsidence. B Volcanol 57, 303-318.

516 Cesca, S., Dahm, T., Juretzek, C., Kuhn, D., 2011. Rupture process of the 2001 May 7 M-w 4.3
517 Ekofisk induced earthquake. Geophys J Int 187, 407-413.

518 Clough, C.T., Maufe, H.B., Bailey, E.B., 1909. The cauldron-subsidence of Glencoe and associated
519 igneous phenomena. J Geol Soc London 64, 611–676.

520 Cundall, P.A., Strack, O.D.L., 1979. A discrete numerical model for granular assemblies.
521 Geotechnique 29, 47-65.

522 Dahm, T., Heimann, S., Bialowons, W., 2011. A seismological study of shallow weak micro-
523 earthquakes in the urban area of Hamburg city, Germany, and its possible relation to salt
524 dissolution. Nat Hazards 58, 1111-1134.

525 Druitt, T.H., Sparks, R.S.J., 1984. On the formation of calderas during ignimbrite eruptions. Nature
526 310, 679 - 681.

527 Ekstrom, G., 1994. Anomalous Earthquakes on Volcano Ring-Fault Structures. Earth Planet Sc Lett
528 128, 707-712.

529 Fichtner, A., Tkalcic, H., 2010. Insights into the kinematics of a volcanic caldera drop: Probabilistic
530 finite-source inversion of the 1996 Bardarbunga, Iceland, earthquake. Earth Planet Sc Lett 297,
531 607-615.

532 Folch, A., Marti, J., 2004. Geometrical and mechanical constraints on the formation of ring-fault
533 calderas. Earth Planet Sc Lett 221, 215-225.

534 Folch, A., Marti, J., 2009. Time-dependent chamber and vent conditions during explosive caldera-
535 forming eruptions. Earth Planet Sc Lett 280, 246-253.

536 Geshi, N., Shimano, T., Chiba, T., Nakada, S., 2002. Caldera collapse during the 2000 eruption of
537 Miyakejima Volcano, Japan. B Volcanol 64, 55-68.

538 Geyer, A., Folch, A., Marti, J., 2006. Relationship between caldera collapse and magma chamber
539 withdrawal: An experimental approach. J Volcanol Geoth Res 157, 375-386.

540 Gudmundsson, A., 1998. Formation and development of normal-fault calderas and the initiation of
541 large explosive eruptions. B Volcanol 60, 160-170.

542 Gudmundsson, A., Marti, J., Turon, E., 1997. Stress fields generating ring faults in volcanoes.
543 Geophys Res Lett 24, 1559-1562.

544 Gutierrez, F., Guerrero, J., Lucha, P., 2008. A genetic classification of sinkholes illustrated from
545 evaporite paleokarst exposures in Spain. Environ Geol 53, 993-1006.

546 Hardy, S., 2008. Structural evolution of calderas: Insights from two-dimensional discrete element
547 simulations. Geology 36, 927-930.

548 Hettema, M.H.H., Schutjens, P.M.T.M., Verboom, B.J.M., Gussinklo, H.J., 2000. Production-
549 Induced Compaction of a Sandstone Reservoir: The Strong Influence of Stress Path.

550 Hildreth, W., Fierstein, J., 2000. Katmai volcanic cluster and the great eruption of 1912. Geol Soc
551 Am Bull 112, 1594-1620.

552 Holohan, E.P., Schopfer, M.P.J., Walsh, J.J., 2011. Mechanical and geometric controls on the
553 structural evolution of pit crater and caldera subsidence. J Geophys Res-Sol Ea 116.

554 Holohan, E.P., Troll, V.R., Errington, M., Donaldson, C.H., Nicoll, G.R., Emeleus, C.H., 2009. The
555 Southern Mountains Zone, Isle of Rum, Scotland: volcanic and sedimentary processes upon an
556 uplifted and subsided magma chamber roof. Geol Mag 146, 400-418.

557 Holohan, E.P., Walter, T.R., Schopfer, M.P.J., Walsh, J.J., de Vries, B.V., Troll, V.R., 2013.
558 Origins of oblique-slip faulting during caldera subsidence. J Geophys Res-Sol Ea 118, 1778-1794.

559 Itacsa Consulting Group Inc., 2004. PFC2D - Particle Flow Code in 2 Dimensions (Version 3.1),
560 3rd ed, Minneapolis, U.S.A.

561 Jaky, J., 1948. Pressure in silos, Proceedings of the 2nd international conference on soil mechanics
562 and foundation engineering, pp. 103-107.

563 Kennedy, B.M., Jellinek, A.M., Stix, J., 2008. Coupled caldera subsidence and stirring inferred
564 from analogue models. Nat Geosci 1, 385-389.

565 Kinscher, J., Bernard, P., Contrucci, I., Mangeney, A., Piguet, J.P., Bigarre, P., 2015. Location of
566 microseismic swarms induced by salt solution mining. Geophys J Int 200, 337-362.

567 Kokelaar, P., 2007. Friction melting, catastrophic dilation and breccia formation along caldera
568 superfaults. J Geol Soc London 164, 751-754.

569 Kumagai, H., Ohminato, T., Nakano, M., Ooi, M., Kubo, A., Inoue, H., Oikawa, J., 2001. Very-
570 long-period seismic signals and caldera formation at Miyake Island, Japan. Science 293, 687-690.

571 Lavallee, Y., de Silva, S.L., Salas, G., Byrnes, J.M., 2006. Explosive volcanism (VEI 6) without
572 caldera formation: insight from Huaynaputina volcano, southern Peru. B Volcanol 68, 333-348.

573 Lavallee, Y., Stix, J., Kennedy, B., Richer, M., Longpre, M.A., 2004. Caldera subsidence in areas of
574 variable topographic relief: results from analogue modeling. J Volcanol Geoth Res 129, 219-236.

575 Legros, F., Kelfoun, K., Marti, J., 2000. The influence of conduit geometry on the dynamics of
576 caldera-forming eruptions. Earth Planet Sc Lett 179, 53-61.

577 Lenhardt, W.A., Pascher, C., 1996. The mechanism of mine-collapse deduced from seismic
578 observations. Pure Appl Geophys 147, 207-216.

579 Lipman, P.W., 1976. Caldera-collapse breccias in the western San Juan Mountains, Colorado. Geol
580 Soc Am Bull 87, 1397-1410.

581 Lipman, P.W., 1984. The roots of ash flow calderas in western North America: Windows into the
582 tops of granitic batholiths. Journal of Geophysical Research: Solid Earth 89, 8801-8841.

583 Marti, J., Ablay, G.J., Redshaw, L.T., Sparks, R.S.J., 1994. Experimental Studies of Collapse
584 Calderas. J Geol Soc London 151, 919-929.

585 Massin, F., Ferrazzini, V., Bachelery, P., Nercessian, A., Duputel, Z., Staudacher, T., 2011.
586 Structures and evolution of the plumbing system of Piton de la Fournaise volcano inferred from
587 clustering of 2007 eruptive cycle seismicity. J Volcanol Geoth Res 202, 96-106.

588 Michon, L., Massin, F., Famin, V., Ferrazzini, V., Roult, G., 2011. Basaltic calderas: Collapse
589 dynamics, edifice deformation, and variations of magma withdrawal. J Geophys Res-Sol Ea 116.

590 Michon, L., Staudacher, T., Ferrazzini, V., Bachelery, P., Marti, J., 2007. April 2007 collapse of
591 Piton de la Fournaise: A new example of caldera formation. Geophys Res Lett 34.

592 Michon, L., Villeneuve, N., Catry, T., Merle, O., 2009. How summit calderas collapse on basaltic
593 volcanoes: New insights from the April 2007 caldera collapse of Piton de la Fournaise volcano. J
594 Volcanol Geoth Res 184, 138-151.

595 Mouginis-Mark, P.J., Robinson, M.S., 1992. Evolution of the Olympus Mons Caldera, Mars. B
596 Volcanol 54, 347-360.

597 Nagel, N.B., 2001. Compaction and subsidence issues within the petroleum industry: From
598 Wilmington to Ekofisk and beyond. Phys Chem Earth Pt A 26, 3-14.

599 Odonne, F., Menard, I., Massonnat, G.J., Rolando, J.P., 1999. Abnormal reverse faulting above a
600 depleting reservoir. Geology 27, 111-114.

601 Pinel, V., 2011. Influence of pre-existing volcanic edifice geometry on caldera formation. Geophys
602 Res Lett 38.

603 Pinel, V., Jaupart, C., 2005. Caldera formation by magma withdrawal from a reservoir beneath a
604 volcanic edifice. Earth Planet Sc Lett 230, 273-287.

605 Potyondy, D.O., Cundall, P.A., 2004. A bonded-particle model for rock. Int J Rock Mech Min 41,
606 1329-1364.

607 Richey, J.E., Thomas, H.H., 1932. The Tertiary ring complex of Slieve Gullion (Ireland). Quarterly
608 Journal of the Geological Society of London 88, 776-849.

609 Robson, G.R., Barr, K.G., 1964. The effect of stress on faulting and minor intrusions in the vicinity
610 of a magma body. B Volcanol 27, 315-330.

611 Roche, O., Druitt, T.H., 2001. Onset of caldera collapse during ignimbrite eruptions. Earth Planet
612 Sc Lett 191, 191-202.

613 Roche, O., Druitt, T.H., Merle, O., 2000. Experimental study of caldera formation. J Geophys Res-
614 Sol Ea 105, 395-416.

615 Sanford, A.R., 1959. Analytical and Experimental Study of Simple Geologic Structures. Geol Soc
616 Am Bull 70, 19-&.

617 Schopfer, M.P.J., Childs, C., Walsh, J.J., 2006. Localisation of normal faults in multilayer
618 sequences. J Struct Geol 28, 816-833.

619 Segall, P., 1989. Earthquakes triggered by fluid extraction. Geology 17, 942-946.

620 Shuler, A., Ekstrom, G., Nettles, M., 2013. Physical mechanisms for vertical-CLVD earthquakes at
621 active volcanoes. J Geophys Res-Sol Ea 118, 1569-1586.

622 Sigmundsson, F., Hooper, A., Hreinsdottir, S., Vogfjord, K.S., Ofeigsson, B.G., Heimisson, E.R.,
623 Dumont, S., Parks, M., Spaans, K., Gudmundsson, G.B., Drouin, V., Arnadottir, T., Jonsdottir, K.,
624 Gudmundsson, M.T., Hognadottir, T., Fridriksdottir, H.M., Hensch, M., Einarsson, P., Magnusson,
625 E., Samsonov, S., Brandsdottir, B., White, R.S., Agustsdottir, T., Greenfield, T., Green, R.G.,
626 Hjartardottir, A.R., Pedersen, R., Bennett, R.A., Geirsson, H., La Femina, P.C., Bjornsson, H.,
627 Palsson, F., Sturkell, E., Bean, C.J., Mollhoff, M., Braiden, A.K., Eibl, E.P.S., 2015. Segmented
628 lateral dyke growth in a rifting event at Bar[eth]arbunga volcanic system, Iceland. Nature 517, 191-
629 195.

630 Staudacher, T., Ferrazzini, V., Peltier, A., Kowalski, P., Boissier, P., Catherine, P., Lauret, F.,
631 Massin, F., 2009. The April 2007 eruption and the Dolomieu crater collapse, two major events at
632 Piton de la Fournaise (La Reunion Island, Indian Ocean). J Volcanol Geoth Res 184, 126-137.

633 Stein, R.S., King, G.C.P., Lin, J., 1994. Stress Triggering of the 1994 M=6.7 Northridge, California,
634 Earthquake by Its Predecessors. Science 265, 1432-1435.

635 Stix, J., Kobayashi, T., 2008. Magma dynamics and collapse mechanisms during four historic
636 caldera-forming events. J Geophys Res-Sol Ea 113.

637 Walters, R.F., 1978. Land subsidence in central Kansas related to salt dissolution. Kansas
638 Geological Survey, University of Kansas, Lawrence.

639 Whittaker, B.N., Reddish, D.J., 1989. Subsidence : occurrence, prediction, and control. Elsevier ;

640 Distributors for the U.S. and Canada, Elsevier Science Pub. Co., Amsterdam, Netherlands ; New
641 York

642 New York, NY, U.S.A.

643 Wilson, C.J.N., Hildreth, W., 1997. The Bishop Tuff: New insights from eruptive stratigraphy. J
644 Geol 105, 407-439.

645

646

647

Tables

Table 1: Properties of particles, bonds and the bulk DEM materials in this study.

Particle Property [a]	**Symbol**	**Value**	**Units**
Maximum radius	r_{max}	10	m
Minimum radius	r_{min}	6	m
Density	ρ	2700	kg m^{-3}
Young's modulus [b]	E_c	1 or 10	GPa
Stiffness ratio (normal to shear)	k_n / k_s	2.5	-
Contact friction coefficient	μ_c	0.5	-
Bond Property [a]	**Symbol**	**Value**	**Units**
Tensile strength [c]	$\overline{\sigma}_c$	1, 5 or 10	MPa
Shear strength [c]	$\overline{\tau}_c$	1, 5 or 10	MPa
Young's modulus [b]	$\overline{E}_c$	1 or 10	GPa
Stiffness ratio (normal to shear)	$\overline{k}_n / \overline{k}_s$	2.5	-
Bond width multiplier	λ	1	-
Bulk Property [a]	**Symbol**	**Value**	**Units**
Young's modulus [d]	E	0.7 – 1.4 or 8 - 12.9	GPa
Poisson's ratio [e]	ν	0.15 – 0.25	-
Unconfined compressive strength [f]	UCS	1.0, 5.0, or 10.5	MPa
Unconfined tensile strength [f]	UTS	0.3, 1.3, or 3.1	MPa
Compressive/Tensile strength ratio	UCS/UTS	2.8 – 3.7	-
Friction coefficient	μ	0.48 – 0.56 [e]	-
Bulk density	ρ	2300 – 2500	kg m^{-3}

650

651 [a] Full definitions of particle and bond properties, as well as details of how the simulated biaxial rock
652 deformation tests are used to calibrate the bulk properties, are given by *Potyondy and Cundall*
653 [2004].

654

655

656 [b] Young's moduli of particles and bonds were always set to be equal in any one model. The Young's
657 moduli of the particles and bonds are scaled to their respective normal stiffness (p. 1336 in
658 [*Potyondy and Cundall, 2004*]).

659

660 [c] Tensile and shear strengths of bonds were always set to be equal in any one model.

661

662 [d] In any one model, as in nature, the bulk Young's Modulus, E, exhibits a slight dependence on
663 depth (i.e. confining pressure). The bulk Young's modulus nonetheless remains in the same order of
664 magnitude as the particle and bond Young's moduli. Thus where particle and bond moduli were set
665 to E = 1 GPa, Young's Modulus increased from E ~ 0.75 GPa near surface to E ~ c. 1.4 GPa at 2
666 km depth. Where particle and bond moduli were set to E_c = 10 GPa, Young's Modulus increased
667 from E ~ 7.5 GPa near surface to E ~ c. 14 GPa at 2 km depth.

668

669 [e] Poisson's ratio, ν, also exhibits a slight depth dependence, and in all models decreased from ν =
670 0.25 near the surface to ν = 0.17 at 2 km depth.

671

672 [f] Unconfined compressive strength (UCS) and unconfined tensile strength (UCS) are closely linked
673 to the bond strength. Models with bond strengths of 1, 5 or 10 MPa typically have bulk UCS values
674 of around 1, 5 or 10 MPa, respectively. UTS values are usually about one third of the respective
675 UCS values.

676

677 ## Figures

678 **Figure 1.** Stress and faulting during caldera collapse. The upper two half-section sketches show
679 existing hypotheses on the relationship of stress to faulting upon magma chamber roof failure. The
680 lower two show fault geometries observed in analog models and in the field. **(A)** An analysis of
681 principal stress directions predicting initial failure along an outward-inclined reverse fault (modified
682 from Anderson, 1936). **(B)** An analysis of differential stress patterns predicting initial failure along
683 an inward-inclined normal fault (modified from Folch and Marti, 2004). **(C)** Analog model showing
684 development of both outward-inclined reverse and inward-inclined normal faults in that order (note
685 numbering of traces) (modified from Roche et al., 2000). **(D)** Interpretation of field and geodetic
686 data for the 2000 collapse of Miyakejima caldera showing development of both outward-inclined
687 reverse and inward-inclined normal faults (modified from Geshi et al., 2002).

688 **Figure 2:** Pre-collapse view of 2D-DEM caldera subsidence models. Note that the light and dark
689 grey layers in the host rock are passive markers for visualization of fault offsets; they do not
690 represent any variation in material properties.

691 **Figure 3:** Schematic sketches of differing structural styles of collapse in the DEM models. In the
692 center is a typical 'single central block' style; end-member styles lie around it. As shown by
693 Holohan et al. (2011), the different styles result from an interaction between geometric or
694 mechanical factors, such as roof thickness/diameter (T/D) ratio, unconfined compressive strength
695 (UCS) and Young's modulus (E). In this article, we focus on the evolution of stress within a
696 representative 'single central block' collapse. Evolutions of stress in the other collapse styles are
697 shown in the Supplementary Material.

698 **Figure 4:** Stress and strain evolution during a typical 'single central block' collapse style. This
699 model has T/D = 0.7, UCS = 5.0 MPa, E= 1.4 GPa (see Table 1 for other properties). Shown
700 column-wise are: the maximum finite shear strain (γ) with black ticks denoting the maximum
701 principal stress directions; the magnitude of the maximum principal stress (σ_1); the magnitude of
702 the minimum principal stress (σ_3); and the magnitude of the maximum shear stress (τ), which is
703 half the differential stress (i.e.,= (σ_1-σ_3)/2). Shown row-wise are stages of the model development
704 with increased percentage of reservoir depletion. Labelling of fractures indicates: T, tensile fracture;
705 R, reverse fault; CR, compression ridge; N, normal fault. Numbering indicates the order of fracture
706 formation. Note the prominent "stress arching" pattern above the reservoir defined by σ_1
707 orientations, σ_1 magnitudes, and the differential stress during the early elastic phase (second row).
708 This stress arching is substantially disrupted, but not totally relaxed (or dissipated), after roof failure
709 along outward-inclined fractures (third row). Note also the outward rotation of σ_1 directions in
710 those areas near the model surface and marginal to the reservoir, where inward-inclined fractures
711 form subsequently (fourth row).

712 **Figure 5:** Principal stress paths during a typical 'single central block' collapse. The inset is a view
713 of the model shown in **Figure 4** with fractures here visualized by shading those particles around

714 which the maximum finite shear strain has exceeded 0.75. Labels of fractures in the inset
715 correspond to those in **Figures 4 and 6A**. The inset also shows the initial (i) and final (f) positions
716 of the circular areas within which a stress path was calculated (note the corresponding colors). In
717 the main figure, a star indicates the starting point of each path (i.e. the initial stress state at depletion
718 = 0%). A large filled circle marks the ending point of each path. Ending points were chosen to
719 balance between a representative view of each path and the clarity of the diagram. Smaller filled
720 circles on each path denote depletion increments of 1%. Numbers and arrows mark points or
721 intervals of depletion at which important stress changes occur. The thick black line labelled $\sigma_1 = \sigma_3$
722 is the isotropic stress axis. The thick black line labelled H-B is a Hoek-Brown failure envelope for
723 the DEM material. Note that most paths reach or come closest to the failure envelope in the
724 compression field. This shows a predominance of shear failure, especially for those fractures most
725 associated with ultimate roof failure (R1 and R2, green and light blue paths, respectively).

726 **Figure 6:** Reservoir unloading-reloading in DEM models of caldera collapse. **(A)** Reservoir
727 pressure vs. depletion in the representative model shown in **Figure 4** (UCS = 5 MPa, solid curve).
728 The vertical grey bars denote pressure changes associated with fracture formation or slip (see
729 **Figures 4 and 5)**. **(B)** Effects of roof thickness/diameter (T/D) ratio on reservoir unloading-
730 reloading (E = 1 GPa, UCS = 5 MPa). Depletion and depressurization (unloading) at collapse onset
731 increase with higher T/D. Also, the amount and sharpness of post-failure reloading decrease. **(C)**
732 Effects of T/D ratio on reservoir unloading-reloading at high Young's modulus (E = 10 GPa, UCS =
733 5 MPa). Note that initial depressurization leading to roof failure occurs over a much shorter
734 depletion interval than in (B). For all plots, reservoir pressure is normalized to the initial pressure at
735 lithostatic equilibrium. Dashed curves in corresponding shades of grey are data from geometrically
736 equivalent models with an 'infinitely strong' host-rock (UCS = 1000 MPa). These show a purely
737 elastic unloading of the reservoir, plus a 'magmastatic' pressure decline. In contrast, the solid

curves also include the effects of non-elastic deformation (i.e. fracturing). Solid sloped lines indicate the depletion-adjusted lithostatic equilibrium (i.e. expected lithostatic-plus-magmastatic pressure in the reservoir) for each T/D ratio.

Figure 7: Influences of geometric and mechanical factors on the critical values of reservoir unloading and depletion at the onset of DEM caldera collapse. Shown column-wise are results from models with low (left) or high (right) Young's Modulus. Plotted against roof thickness/diameter ratio (T/D) are: (top row) the critical percentage of reservoir depletion, (middle row) the corresponding drop in pressure - i.e. unloading - of the reservoir from the initial lithostatic-plus-magmastatic value and (bottom row) the critical reservoir pressure normalized to the initial value. Symbols denote results of models with differing unconfined compressive strengths (UCS). See main text for further explanation.

Figure 8: End-member principal stress paths leading to reservoir roof failure. (A) Minimum stress remains constant while maximum stress increases; (B) Maximum stress remains constant while minimum stress decreases; (C) Differential stress stays constant, but mean stress decreases; (D) Mean stress stays constant, but differential stress increases. Each end-member path is illustrated in principal stress space (left) and in Mohr space (right). HB = Hoek-Brown failure envelope. Stress path colors correspond to those of the observed paths in Figure 5. Stress paths typically start from a line $\sigma_1 = k\sigma_3$, where k is the inverse of the coefficient of lateral earth pressure at rest (Jaky, 1948). As shown diagrammatically here, certain parts of the reservoir roof generally display particular end-member stress paths. In some parts of the roof, a mix of end-members may occur, depending on roof geometry, material strength, and stress changes induced by progressive deformation (see Figure S9 for examples). For ultimate failure of the roof, the stress path in (D) is generally the most significant.

Figure 9: Summary of stress evolution during a single central block caldera collapse. Darkly shaded areas in the initial elastic phase show the end-member stress paths to failure. Central roof failure along outward-dipping reverse faults leads to the partial relaxation of the stress arch and to the outward rotation of the principal stress directions in the peripheral zone. This outward rotation, combined with a transfer of differential stress from the central zone to the periphery, leads to the formation of inward-dipping normal faults here. The reservoir undergoes an initial unloading of the roof-related stresses, but roof failure leads to a reloading of the reservoir. Friction within the down-going roof causes a persistence of the stress arching and so may inhibit re-establishment of the full roof load onto the reservoir.

Text to Supplementary Material of

"Stress Evolution during Caldera Subsidence"

by E.P. Holohan, M.P.J Schöpfer & J.J. Walsh

S1. Tests for effects of changing model boundary conditions and resolution

S1.1 External boundaries

The external boundaries in the models of the main article are cohesion- and frictionless. This choice of boundary condition is somewhat arbitrary, since as long as the 'box' defined by the boundary walls is large enough, the boundaries have little effect on the model outcome. This is demonstrated in **Figures S1 and S2**, which show that the effects of enlarging the box or of imposing opposite end-member (i.e. fully-fixed) external boundary conditions on the host-rock stress paths and the reservoir stresses are minimal.

S1.2 Reservoir/host-rock interface

In the main article, the boundary condition at the sill-host rock interface is frictional and cohesion-less. In the limit, settling 'magma' particles can detach from the reservoir ceiling and walls; this may be possible for magma in nature due to gas exsolution. The coefficient of friction at the boundary is nominally that of the reservoir particles, i.e. 0.01, although, as explained below, this may locally increase due to particle interlocking. These boundary conditions facilitate a simple but numerically robust approximation of fluid-like behaviour in the reservoir, in that the particles can "flow" due to differential stress.

As shown in **Figure S2**, the 'magma' stress state is not isotropic (or 'hydrostatic'), but is characterised by a small non-zero differential stress (between 1-5 MPa). This differential stress ultimately drives flow of the particles. It arises in large part because the confined low-friction particles seek to rearrange to an ideal (closest) packing, such that flow is resisted by the particle framework itself. This 'framework effect' and the differential stress related to it are independent of the particle contact friction. Consequently, and a shown on **Figures S1 and S2**, reducing the reservoir particle friction by three orders of magnitude has little effect on the stress evolution in either the reservoir or the host-rock.

An alternative ‘welded’ reservoir-host rock boundary condition is effectively assumed in many past continuum-based numerical modelling studies of magma chamber depletion – e.g. (Gudmundsson et al 1997; Folch and Marti 2004; Holohan et al., 2013). We tested a simplified, extreme version of such a no-slip ‘super-bonded’ boundary condition by setting no-slip contact bonds (Itasca Consulting Group 2004) of ‘infinitely’ high strength between the reservoir particles and between the particles at the host-rock/reservoir interface.

As shown in **Figure S3a**, this ‘super-bonded’ boundary condition nonetheless produces a very similar stress pattern in the elastic phase (i.e. at low depletions - here 5%) to that seen with what is essentially the opposite end-member boundary condition in the models of the main text (see **Figure 4**). Differences become more pronounced at higher depletions, with the ‘super-bonded’ condition producing anomalously high strains in the host rock immediately adjacent the reservoir. This leads to a difference in the position of reverse faulting associated with failure – in the models with the ‘super-bonded’ reservoir condition, the reverse faults initiate at the edges of the high strain zone in the host rock rather than at the edges of the reservoir. Nonetheless, the stress paths for the fractures in the cover (i.e. reservoir roof) in the super-bonded case are essentially the same as those in the ‘standard’ model (See **Figure S3b**). The only exception is for the area immediately above the reservoir. Here, the stresses in the super-bonded case are linked to an effect of the boundary condition – effectively the reservoir is being modelled as a uniformly contracting solid such that it exerts very high shear stresses against the host rock as it reduces in area. Another effect of this solid behaviour is that the reservoir ‘pressure’ (mean stress) can attain highly negative absolute values – something very unlikely to characterise a magma reservoir in nature (**Figure S3c**).

Another more complex approach to simulating the host-rock-boundary interface would be to apply particle forces normal to the interface. The simplest implementation, assigning a radially-inward direction to the forces (e.g. Alassi et al., 2003), would likely result in over-constraining the reservoir behaviour. A more complex implementation allowing for free movement of the reservoir-host rock interface under gravity would face difficulty in remaining numerically stable at high depletions (and strains) and would possibly require coupling to a finite element or boundary element code, which is beyond the technical scope of our study. Moreover, it would be unlikely to change our broader conclusions, given the general similarities of model host rock behaviour even with the diametrically differing end-member boundary conditions tested here.

S1.3 Particle resolution

The model resolution in the main article was chosen to provide a reasonable balance between the structural resolution of faults etc., and the model run time for the model scale. For the resolution used here, with particle radii between 6-10m and comprising 50,000 particles, model run time on a fairly powerful desktop machine (3.6 GHz processor, 32 Gb RAM) was typically over 24 hours. We also tested the effects of increased model resolution by running models of equivalent size, but with particles radii between 3-5m and 1.8 – 3m. These comprised over 200,000 and 500,000 particles, respectively. The run time for one model to 50% depletion, equivalent to that in the 'low resolution' models, took over 7 and 50 days respectively. Thus it was unfeasible time-wise for us to have fully explored the parameter space presented in the paper, which is covered by 74 individual model realisations including multiple realisations for each parameter combination, at such high particle resolutions.

Moreover, the faults developed in higher resolution test models are actually quite similar in terms of orientation and position to those in the 'low resolution' models of the paper (**Figure S4a**). The main and unsurprising difference is that fault zone width decreases with decreasing particle size. Also the pattern of stress paths is almost identical to that in the low resolution models (**Figure S4b**). A subtle effect of higher particle resolution is a slight decrease in the pressure drop or depletion required to initiate ultimate roof failure and a slightly increased post-failure reloading (**Figure S4c**). These effects can be attributed to a reduced fracture toughness of the material at higher particle resolutions (Potyondy and Cundall, 2004). Such effects are likely to be systematic across all model geometries, however, and so are unlikely to change the general findings made from the lower resolution models in the main article.

S2. Variations in results associated with changes in model parameters

Here we summarise the evolutions of stress and fracturing within other collapse styles seen in the DEM model results (**Figure 3)**. These other collapse styles arise from varying the mechanical (UCS, E) and geometric (T/D) parameters of the reservoir roof. As noted in the main text, the main features of the stress evolutions in these cases are actually rather similar to that of the representative 'single central block collapse' model, and so here we focus more on the differences. We also show here in some more detail how variation in the model's

geometric and mechanical parameters affects the unloading-reloading of the reservoir and the amount of depletion or 'under-pressure' needed to cause ultimate roof failure.

S2.1 Stress and strain evolution in end-member collapse styles

A sufficiently shallow reservoir (T/D < 0.3) favours 'central sagging' or 'central snapping' collapse styles. 'Central sagging' occurs with low host-rock strength (**Figure S5**); 'Central snapping' occurs with high host-rock strength (**Figure S6**).

The main difference in both cases from the representative model (**Figure 4)** is that the initial elastic phase of subsidence is marked by a zone of especially high σ_1 and differential stress magnitudes in the central upper part of the roof. Indeed, the overall differential stress pattern is very similar to that shown in **Figure 1B**, which has been previously interpreted to lead to initial formation of an inward-dipping normal fault (Folch and Marti 2004). In both DEM models, however, the initially-formed structures comprise a pop-up structure or compressional ridge in the roof's near-surface central area, plus outward-dipping fractures in the roof's lower marginal areas.

A sufficiently deep reservoir (T/D < 1.0) favours either a "quasi-single central block" or a "multiple central block" collapse style. The former occurs with low strength and/or high Young's modulus (**Figure S7**); the latter occurs with high strength and/or low Young's modulus (**Figure S8**). The main difference from the representative model (**Figure 4)** is that in both cases the pattern of stress arching above the reservoir is disrupted through an upward-migrating sequence of material failures. At high modulus, this migration occurs very rapidly in depletion terms, such that very little strain accumulates on the failure-related fractures at depth (**Figure S7**). At low modulus, the migration occurs more slowly in depletion terms, such that strain accumulation on the failure-related fractures at depth leads to number of well-defined blocks (**Figure S8**).

The similarities of stress and fracturing evolutions in the end-member collapse styles and in the representative model are nevertheless strong. In all cases, stress arches and stress bowls develop in the elastic phase. The formation of fractures accommodating horizontal contraction (pop-up structures and/or outward-dipping reverse faults) again marks the disruption of the stress arch. Stress arch disruption leads to outward rotation of principal stress trajectories in the upper marginal parts of the roof and transfer of differential stress to these parts. Major fractures accommodating horizontal extension (inward-dipping normal faults)

eventually form here. Finally, and although more weakly so in the low T/D models, stress arching persists within the subsiding roof after its ultimate failure in all cases.

S2.2 Stress paths in end-member collapse styles

Figure S9 shows that stress paths taken toward fracture in the end-member collapse styles also differ only subtly from those in the representative model (**Figure 5**). The most notable difference occurs in the low T/D models, where the stress paths in the roof's lower marginal areas move toward the failure envelope at steeper, non-perpendicular orientations to the isostatic line (light blue and green paths in **Figure S9 A,B)**. This effect is most pronounced in the high-strength "central snapping" style. One explanation for this difference may be that the marginal areas of such thin roofs are subject to higher bending stresses, which are added mainly to the generally more-horizontally orientated σ_1 (**Figure S6**).

In the high T/D models, the main difference to the representative stress paths shown in **Figure 5** is an additional path for the roof centre (yellow path in **Figure S9 C,D**) where fracturing occurs to delimit the upper part of a detached block. With respect to the isostatic line, motion along this path is initially near-perpendicular, but then abruptly switches to be near-parallel, followed by a retreat. This abrupt switch is associated with the upward passage of the failure zones in such thick roofs. In all other respects, the stress paths in the end-member collapse styles are very similar to those in the representative model.

S2.3 Relationship of near-surface tensile fracturing to roof failure

Figure S10 shows further details of the relationship of fracturing or slip events to the reservoir 'pressure' evolution in DEM models. The plots for three selected models are arranged in order of increasing T/D ratio, and they correspond to the 'central snapping', 'single central block' and 'multiple central block' collapse styles shown in **Figures S6, 4 and S8**, respectively.

Figure S10a shows that initial formation of near-surface tensile fractures (T1 and T2) marks neither (1) the ultimate failure of the roof nor (2) the concurrent formation of an inward-dipping normal ring fault. This is despite the fact that the stress pattern in the elastic phase of this model (**Figure S6**) is very similar to that previously interpreted as leading to both these outcomes (**Figure 1b**) (Folch and Marti 2004). Rather, ultimate roof failure occurs here in association with the formation of the pop-up structure in the roof centre (CR) and an outward-dipping reverse fault (R1) just above the reservoir margin. **Figure S10b**, which is the

same as that in **Figure 6a** and is included here for reference, makes essentially the same point as **Figure 6a**. Initial tensile fracturing in these examples hence marks a yielding ('cosmetic failure') of the roof material.

Figure S6c shows that with increased T/D, the yielding phase is no longer associated with formation of near-surface tensile fractures, but with distributed deformation and the formation of minor reverse faults (R1 and R2) immediately above the reservoir. Again, ultimate roof failure is associated with the formation of outward-inclined reverse faults (R3 and R4), and in this case it precedes the formation of a depression at the surface. Collapse through to surface is marked by the formation of another reverse fault (R5). At this point, the first surface tensile fracture (T1) forms. After a further period of depletion, another reverse fault (R6), several surface tensile fractures (T2-T4) and an inward inclined normal fault (N1) develop in quick succession.

With high T/D, near surface tensile fracturing therefore occurs after ultimate roof failure, rather than marking it. Moreover, and in agreement with some past interpretations for such a roof geometry (Folch and Marti 2004, Holohan et al. 2013), surface tensile fracturing occurs either with or after onset of surface collapse marked by the initial formation of outward-dipping reverse faults rather than inward-dipping faults.

S2.4 Effects of parameter variations on reservoir unloading-reloading

As noted and explained in the main text, the reservoir unloading-reloading history is most strongly affected by the roof's T/D ratio and it's Young's modulus (**Figures S11)**.

With respect to the initial unloading phase, and all other parameters being equal, increasing the roof's T/D ratio increases the maximum reservoir under-pressure (i.e. the magnitude of reservoir unloading) sustained by the roof. Increasing the roof's unconfined strength has a similar effect, although this is not so pronounced at the highest T/D values (see main text for explanation). The plots here further show that the amount of depletion required to reach ultimate roof failure also increases with increased T/D ratio. From the plots in **Figure S11,** one might be tempted to suggest that this critical depletion may also increase with increased strength (all other parameters being equal). This relationship is unclear when all the available data are examined, however (see **Figure 7**). The main effect of increased Young's modulus is to increase the rapidity, in depletion terms, of the initial unloading. This effect is further shown here for a variety of roof T/D and strength values (**Figure S11)**.

With respect to the post-failure reloading phase, the strongest effect stems from the roof's T/D ratio (**Figure S11)**. At low T/D, the post-nadir reloading of the reservoir is sharp. With increased T/D, the post-nadir reloading is increasingly gradual. A similarly increased sharpness of post-failure reloading is also seen with higher roof strength, albeit more so for low T/D values. These patterns largely reflect a more brittle failure of the roof at low T/D and high strengths vs. a more ductile failure at high T/D and low strengths. Finally, as noted in the main text, and shown here for a variety of strength and modulus values, the post-failure reservoir pressure returns to a depletion-adjusted lithostatic value for low T/D only. The post failure reservoir pressure remains progressively further below the lithostatic value (i.e. the magnitude of reloading is inhibited) as T/D increases.

Additional references:

Alassi, H.T.I., L. Liming, R.M. Holt, (2006), Discrete Element Modeling of Stress and Strain Evolution Within and Outside a Depleting Reservoir, *Pure Appl. Geophys*. 163, 1131-1151.

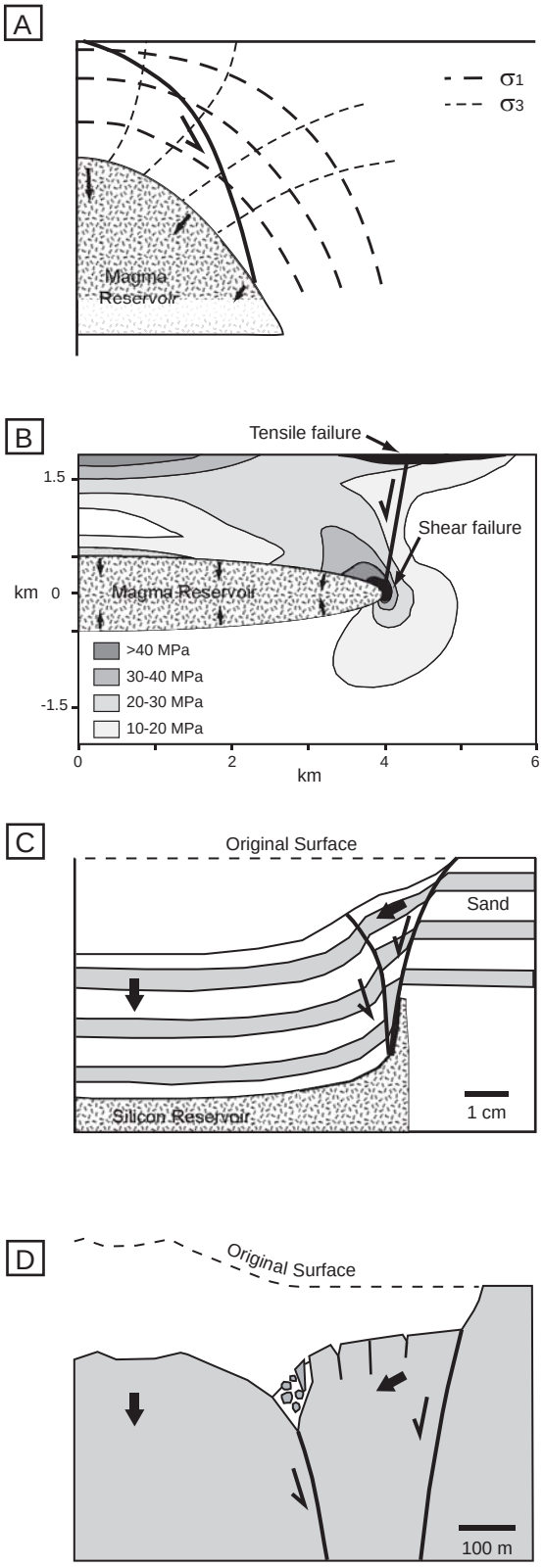

Figure 1: Stress and faulting during caldera collapse. The upper two half-section sketches show existing hypotheses on the relationship of stress to faulting upon magma chamber roof failure. The lower two show fault geometries observed in analog models and in the field. (A) An analysis of principal stress trajectories predicting initial failure along an outward-inclined reverse fault (modified from Anderson, 1936). (B) An analysis of differential stress patterns predicting initial failure along an inward-inclined normal fault (modified from Folch and Marti, 2004). (C) Analog model showing development of both outward-inclined reverse and inward-inclined normal faults in that order (note numbering of traces) (modified from Roche et al., 2000). (D) Interpretation of field and geodetic data for the 2000 collapse of Miyakejima caldera showing development of both outward-inclined reverse and inward-inclined normal faults (modified from Geshi et al., 2002).

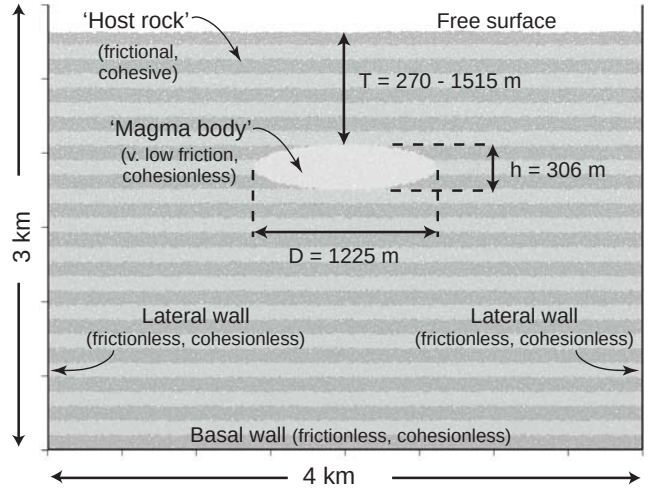

Figure 2: Pre-collapse view of 2D-DEM caldera subsidence models. Note that the light and dark grey layers in the host rock are passive markers for visualization of fault offsets; they do not represent any variation in material properties.

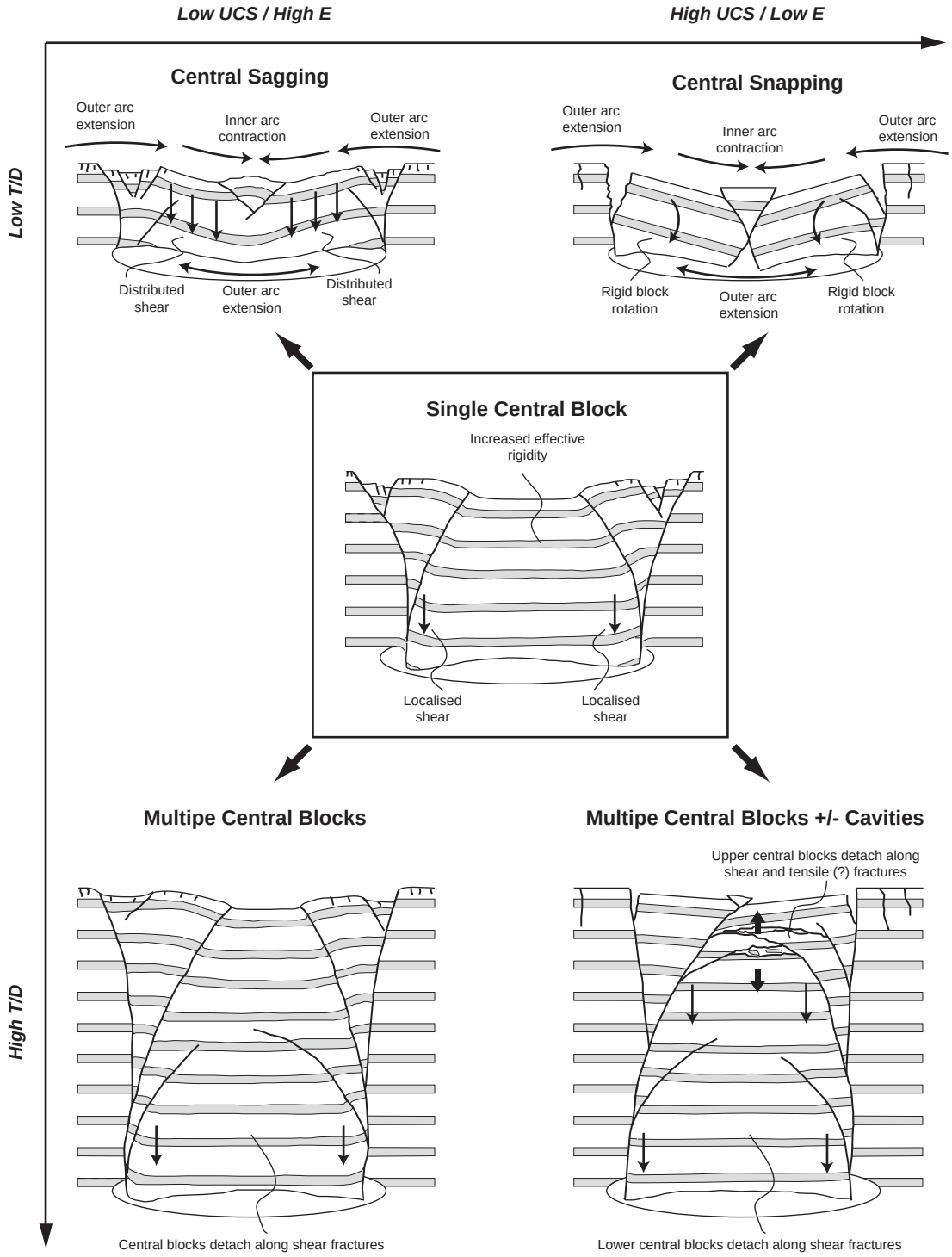

Figure 3. Schematic sketches of differing structural styles of collapse in the DEM models. Shown in the center is a typical ‘single central block’ style with end-member styles around it. As shown by Holohan et al. (2011), the different styles result from an interaction between geometric or mechanical factors, such as roof thickness/diameter (T/D) ratio, unconfined compressive strength (UCS) and Young’s modulus (E). In this article, we focus on the evolution of stress within a representative ‘single central block’ collapse. Evolutions of stress in the other collapse styles are shown in the Supplementary Material.

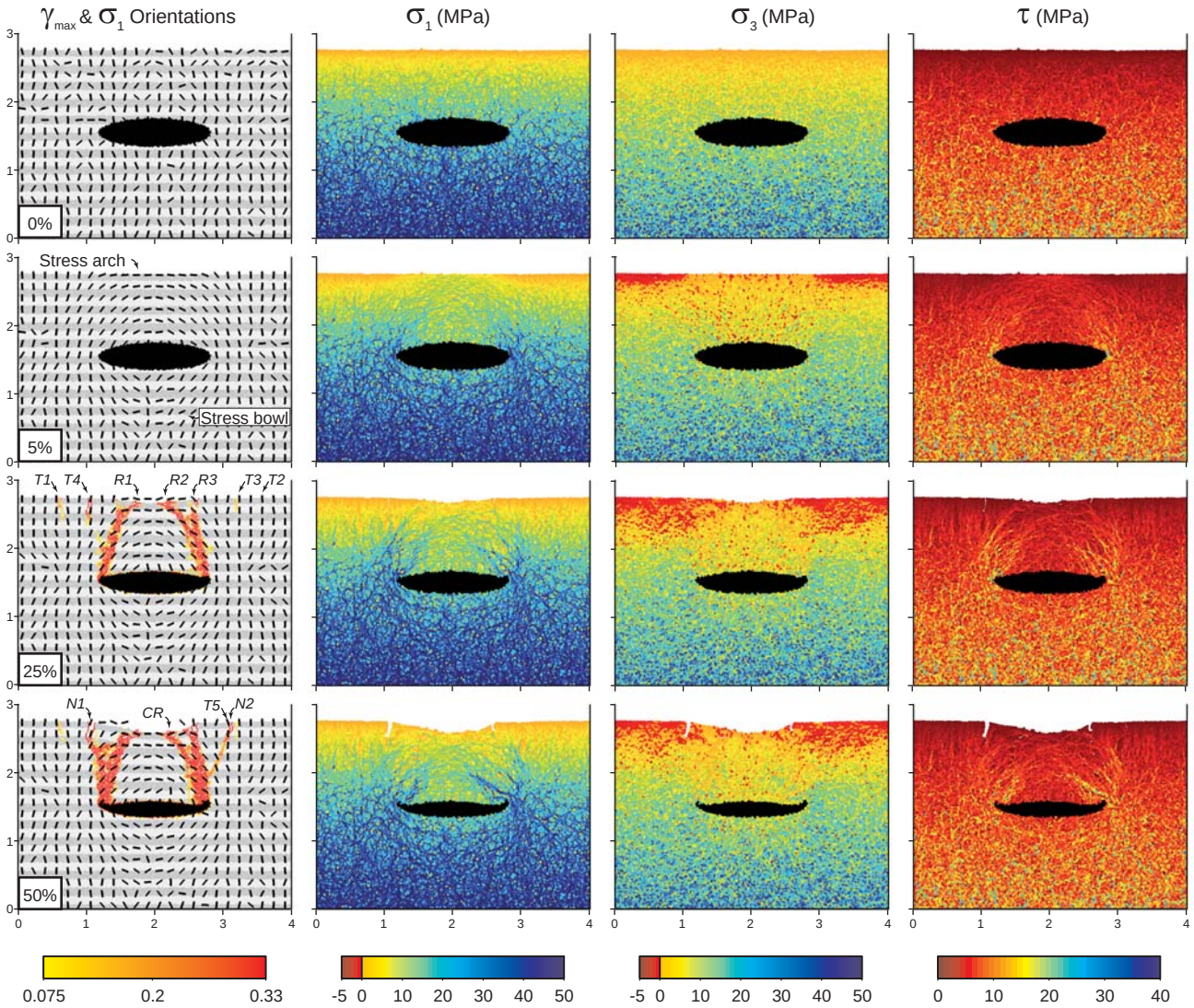

Figure 4: Stress and strain evolution during a typical 'single central block' collapse style. This model has T/D = 0.7, UCS = 5.0 MPa, E= 1.4 GPa (see Table 1 for other properties). Shown columnwise: the maximum finite shear strain (γ_{max}) with black ticks denoting the maximum principal stress orientations; the magnitude of the maximum principal stress (σ_1); the magnitude of the minimum principal stress (σ_3); and the magnitude of the maximum shear stress (τ) (differential stress (= (σ_1-σ_3)/2)). Shown row-wise are stages of the model development as the percentage reservoir depletion increases. Labelling of fractures indicates: T, tensile fracture; R, reverse fault; N, normal fault. Numbering indicates order of formation. Note the prominent "stress arching" pattern above the reservoir defined by σ1 orientations, σ_1 magnitudes, and the differential stress during the initial elastic phase (second row). This stress arching is substantially disrupted, but not totally relaxed, after roof failure along outward inclined faults (third row). Note also the post-failure outward rotation of σ_1 trajectories in those areas near the model surface and marginal to the reservoir, where later inward-inclined faults form (fourth row).

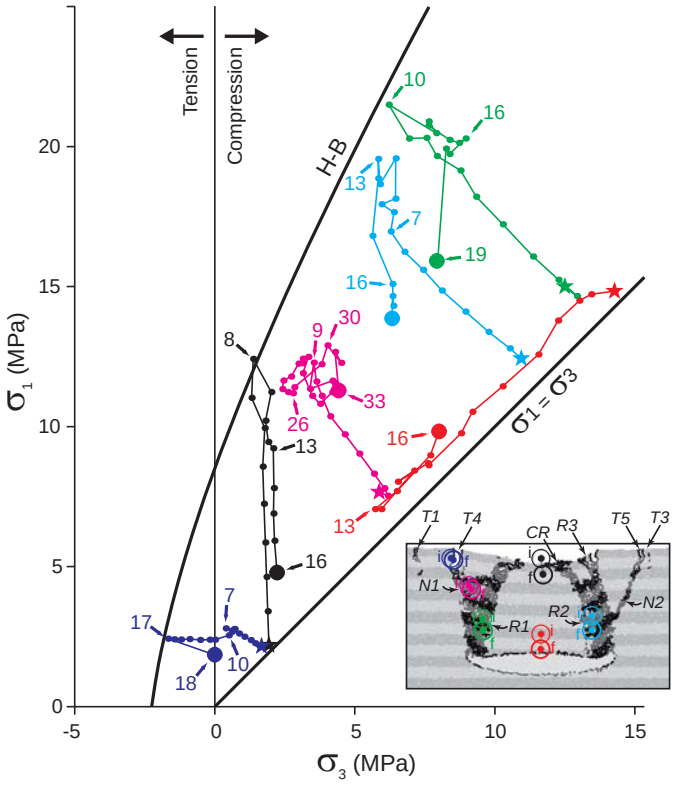

Figure 5: Principal stress paths during a typical 'single central block' collapse. The inset is a view of the model shown in Figure 4 with fractures here visualized by shading those particles around which the maximum finite shear strain has exceeded 0.75. Labels of fractures in the inset correspond to those in Figures 4 and 6A. The inset also shows the initial (i) and final (f) positions of the circular areas within which a stress path was calculated (note the corresponding colors). In the main figure, a star indicates the starting point of each path (i.e. the initial stress state at depletion = 0%). A large filled circle marks the ending point of each path. Ending points were chosen so as to balance between a representative view of each path and the clarity of the diagram. Smaller filled circles on each path denote depletion increments of 1%. Numbers and arrows mark points or intervals of depletion at which important stress changes occur. The thick black line labelled $\sigma_1 = \sigma_3$ is the isotropic stress axis. The thick black line labelled H-B is a Hoek-Brown failure envelope for the DEM material. Note that most paths reach or come closest to the failure envelope in the compression field. This shows a predominance of shear failure, especially for those fractures most associated with ultimate roof failure (R1 and R2, green and light blue paths, respectively).

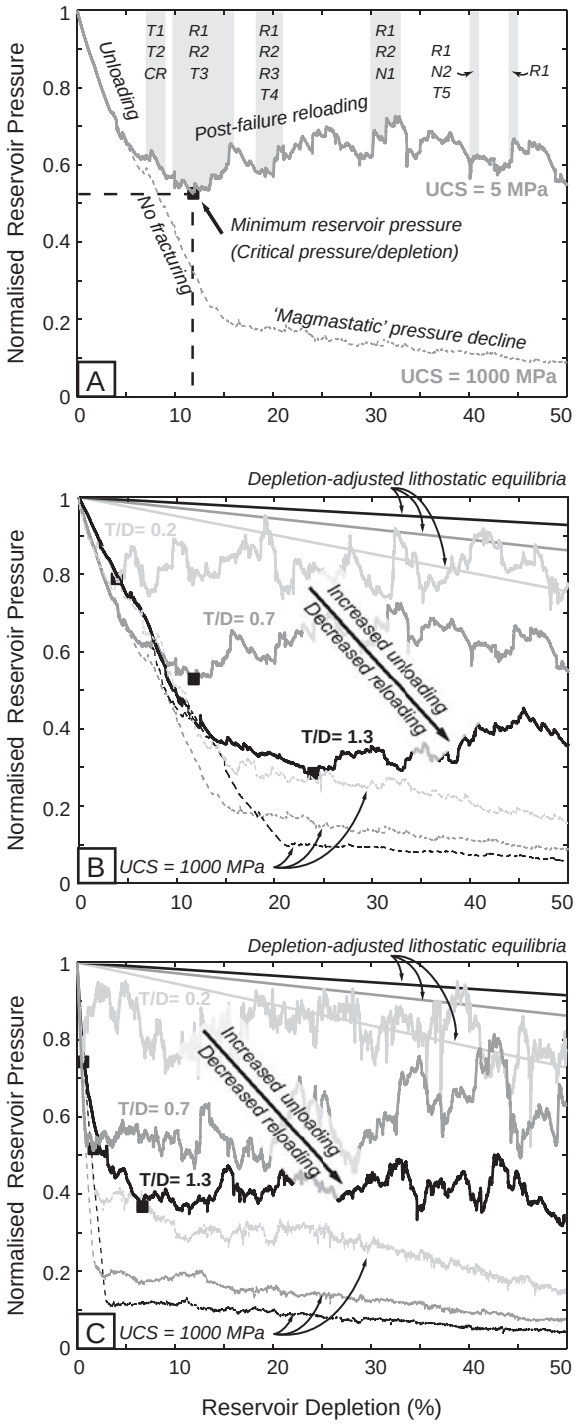

Figure 6: Reservoir unloading-reloading in DEM models of caldera collapse. ***(A)*** Reservoir pressure vs. depletion in the representative model shown in Figure 4 (UCS = 5 MPa, solid curve). The vertical grey bars denote pressure changes associated with fracture formation or slip (see Figures 4 and 5). ***(B)*** Effects of roof thickness/diameter (T/D) ratio on reservoir unloading-reloading (E = 1 GPa, UCS = 5 MPa). Depletion and depressurization (unloading) at collapse onset increase with higher T/D. Also, the amount and sharpness of post-failure reloading decrease. ***(C)*** Effects of T/D ratio on reservoir unloading-reloading at high Young's modulus (E = 10 GPa, UCS = 5 MPa). Note that initial depressurization leading to roof failure occurs over a much shorter depletion interval than in (B). For all plots, reservoir pressure is normalized to the initial pressure at lithostatic equilibrium. Dashed curves in corresponding shades of grey are data from geometrically equivalent models with an 'infinitely strong' host-rock (UCS = 1000 MPa). These show a purely elastic unloading of the reservoir, plus a 'magmastatic' pressure decline. In contrast, the solid curves also include the effects of non-elastic deformation (i.e. fracturing). Solid sloped lines indicate the depletion-adjusted lithostatic equilibrium (i.e. expected lithostatic-plus-magmastatic pressure in the reservoir) for each T/D ratio.

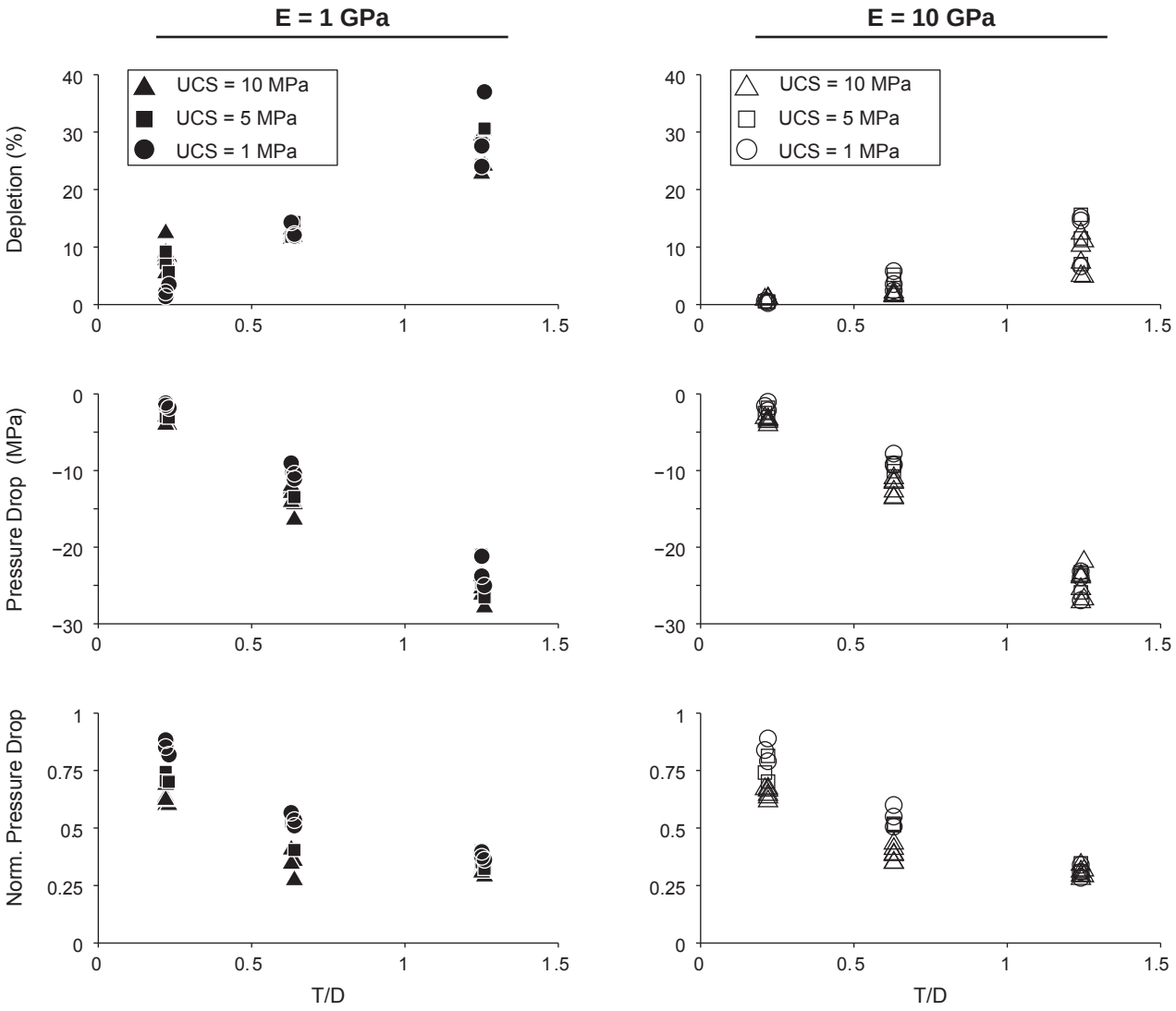

Figure 7: Influences of geometric and mechanical factors on the critical values of reservoir unloading and depletion at the onset of DEM caldera collapse. Shown column-wise are results from models with low (left) or high (right) Young's Modulus. Plotted against roof thickness/diameter ratio (T/D) are: (top row) the critical percentage of reservoir depletion, (middle row) the corresponding drop in pressure - i.e. unloading - of the reservoir from the initial lithostatic-plus-magmastatic value and (bottom row) the critical reservoir pressure normalized to the initial value. Symbols denote results of models with differing unconfined compressive strengths (UCS). See main text for further explanation.

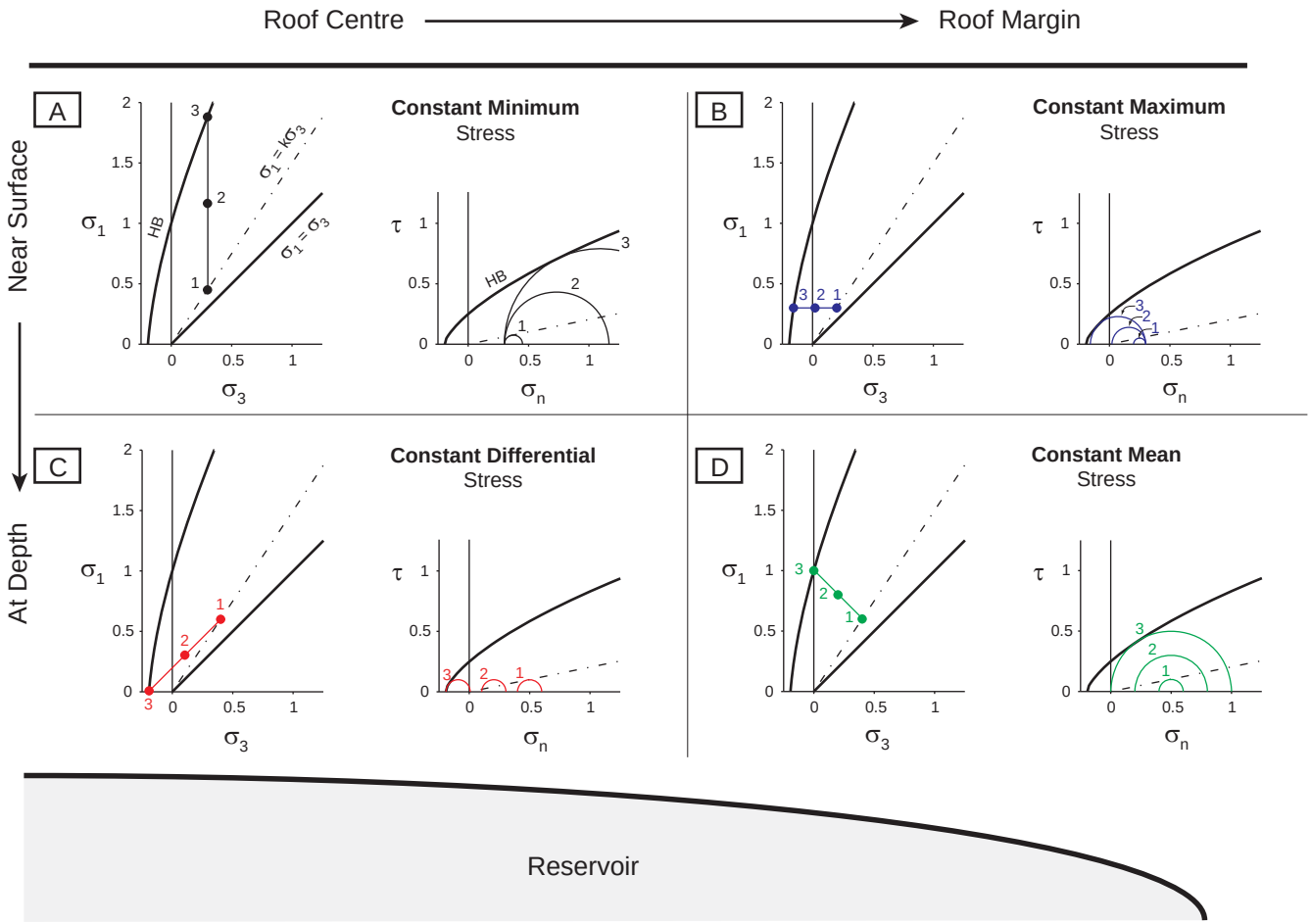

Figure 8: End-member principal stress paths leading to reservoir roof failure. (A) Minimum stress remains constant while maximum stress increases; (B) Maximum stress remains constant while minimum stress decreases; (C) Differential stress stays constant, but mean stress decreases; (D) Mean stress stays constant, but differential stress increases. Each end-member path is illustrated in principal stress space (left) and in Mohr space (right). HB = Hoek-Brown failure envelope. Stress path colors correspond to those in Figure 5. As shown diagrammatically here, certain parts of the reservoir roof generally display particular end-member stress paths. In some parts of the roof, a mix of end-members may occur, depending on roof geometry, material strength, and stress changes induced by progressive deformation (see Figure S9 for examples). For ultimate failure of the roof, the stress path in (D) is generally the most significant.

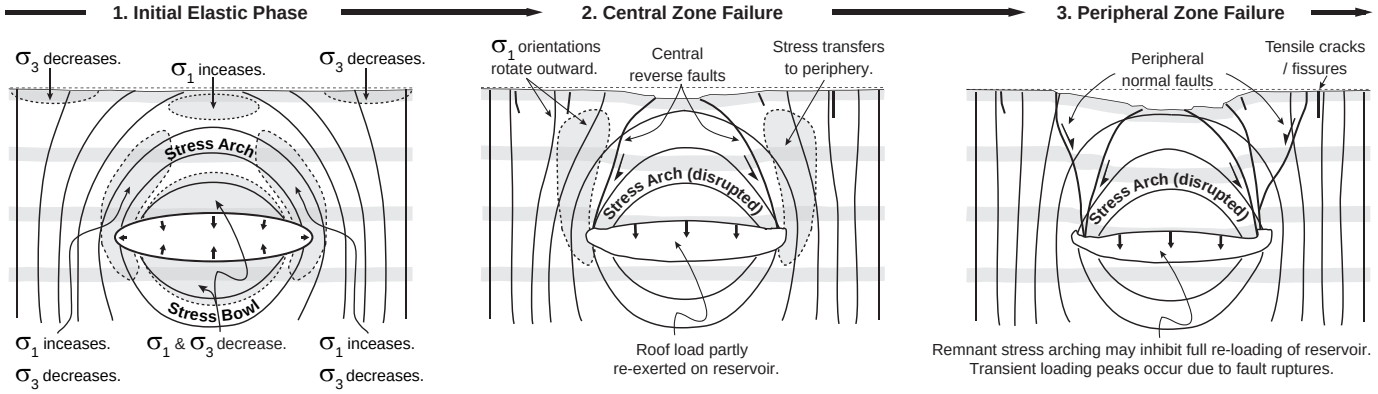

Figure 9: Summary of stress evolution during a single central block caldera collapse. Darkly shaded areas in the initial elastic phase show the end-member stress paths to failure. Central roof failure along outward-dipping reverse faults leads to the partial relaxation of the stress arch and to the outward rotation of the principal stress orientations in the peripheral zone. This outward rotation, combined with a transfer of differential stress from the central zone to the periphery, leads to the formation of inward-dipping normal faults here. The reservoir undergoes an initial unloading of the roof-related stresses, but roof failure leads to a reloading of the reservoir. Friction within the down-going roof causes a persistence of the stress arching and so may inhibit re-establishment of the full roof load onto the reservoir.

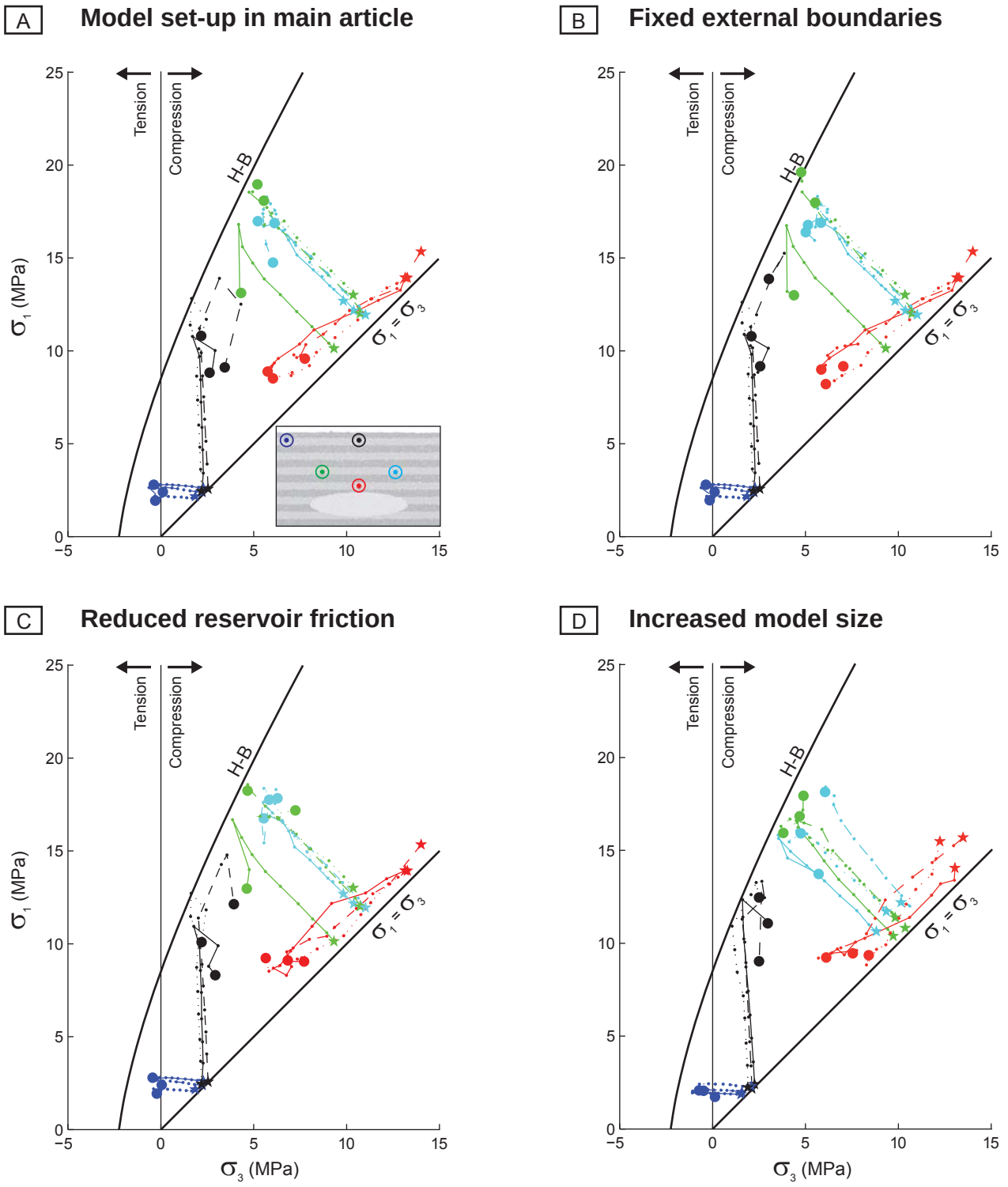

Figure S1: Test for effects of boundary conditions on stress paths. **(A)** Paths from three realisations of the representative model set-up in this paper. This has non-cohesive, frictionless external boundaries; has reservoir particle friction = 0.01; and has boundary dimensions of 3 x 4 km. **(B)** Paths from realisations with fixed external boundaries. **(C)** Paths from realisations with reservoir friction reduced to 0.00001. **(D)** Paths from realisations with boundary dimensions increased to 5 x 15 km. All paths span a depletion of 0-10%. Each plot contains data from three model realisations (i.e. particle assemblages). The dotted lines in (A) are data from the representative model of the main article. Inset in (A) shows the initial locations of the circular areas for which the paths were calculated. These are the same for the models in all figure parts. See caption to Figure 5 for further explanation of symbols and labels.

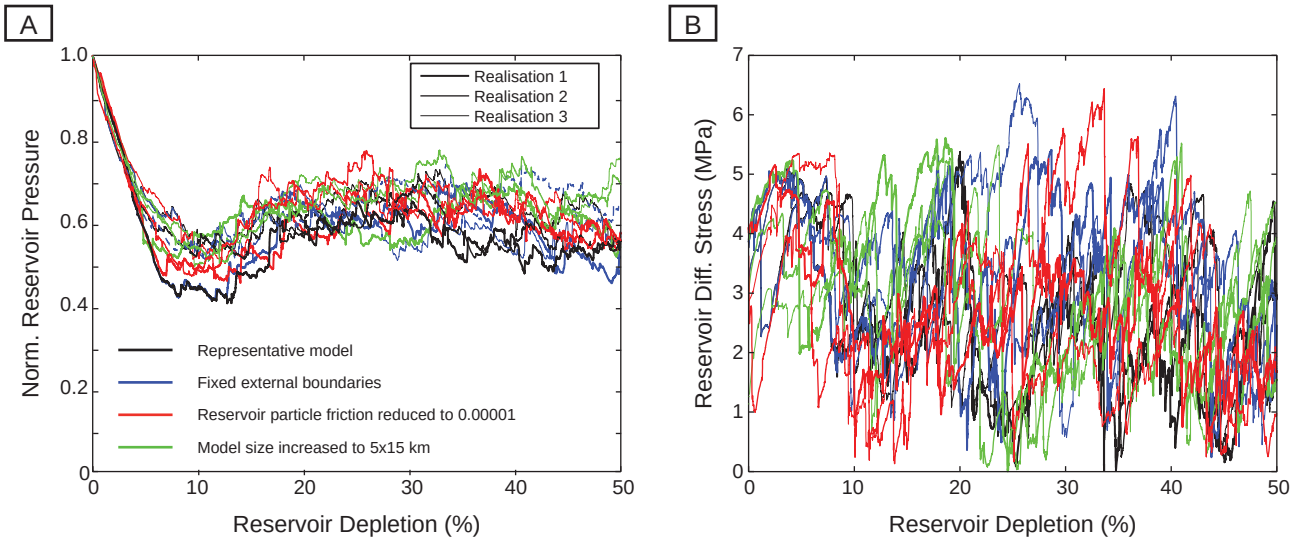

Figure S2: Test for effect of boundary conditions on reservoir stresses: **(A)** Reservoir mean stress, i.e. reservoir pressure, **(B)** Reservoir differential stress. The legend in part (A) applies also to part (B). Results from three model realisations (i.e. particle assemblages) are shown for each configuration of boundary conditions. Note that the curves from each configuration overlap substantially with, or lie within the range of, those of other configurations. This implies that effects from changing the boundary conditions as done here are minimal.

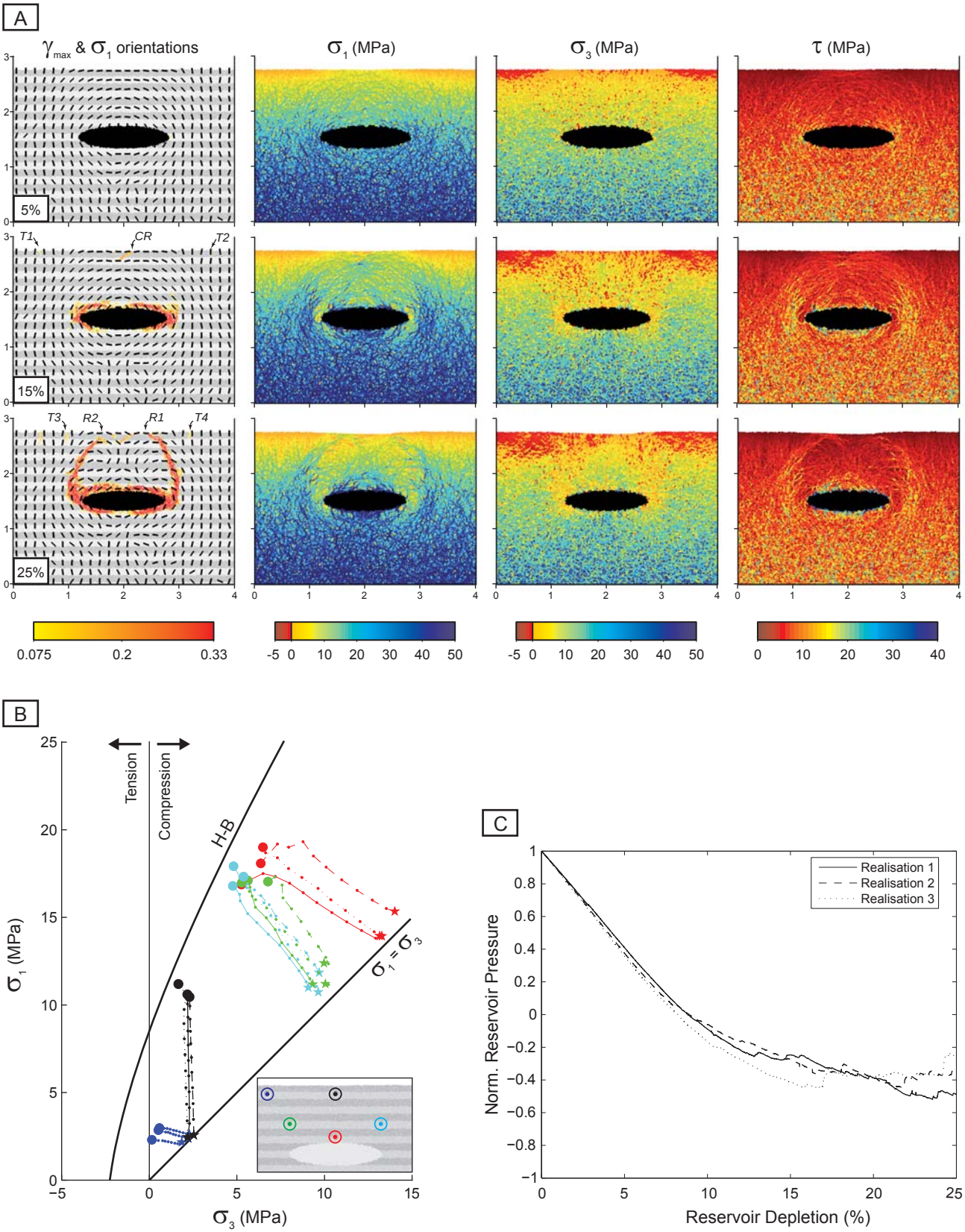

Figure S3: Effects of infinitely-strong contact bonding of reservoir particles to each other and to the host-rock. **(A)** Stress and strain evolution. Host-rock properties are the same as in Figure 4. See caption to Figure 4 for explanation of layout and annotations. Note the development of large shear stresses in the host-rock immediately above and below the reservoir. **(B)** Stress paths for three model realisations run up to 10% depletion. See caption to Figure 5 for explanation of labels and symbols. Inset shows the initial positions of the circular areas for which each path was calculated. None of the paths reach failure by 10% depletion, probably because of the concentration of strain around the reservoir. Only the red stress path (area immediately above the reservoir centre) deviates from the orientations in Figure 5. **(C)** Evolution of reservoir pressure (normalised to maximum). Note that the pressure (mean stress) declines to large negative values.

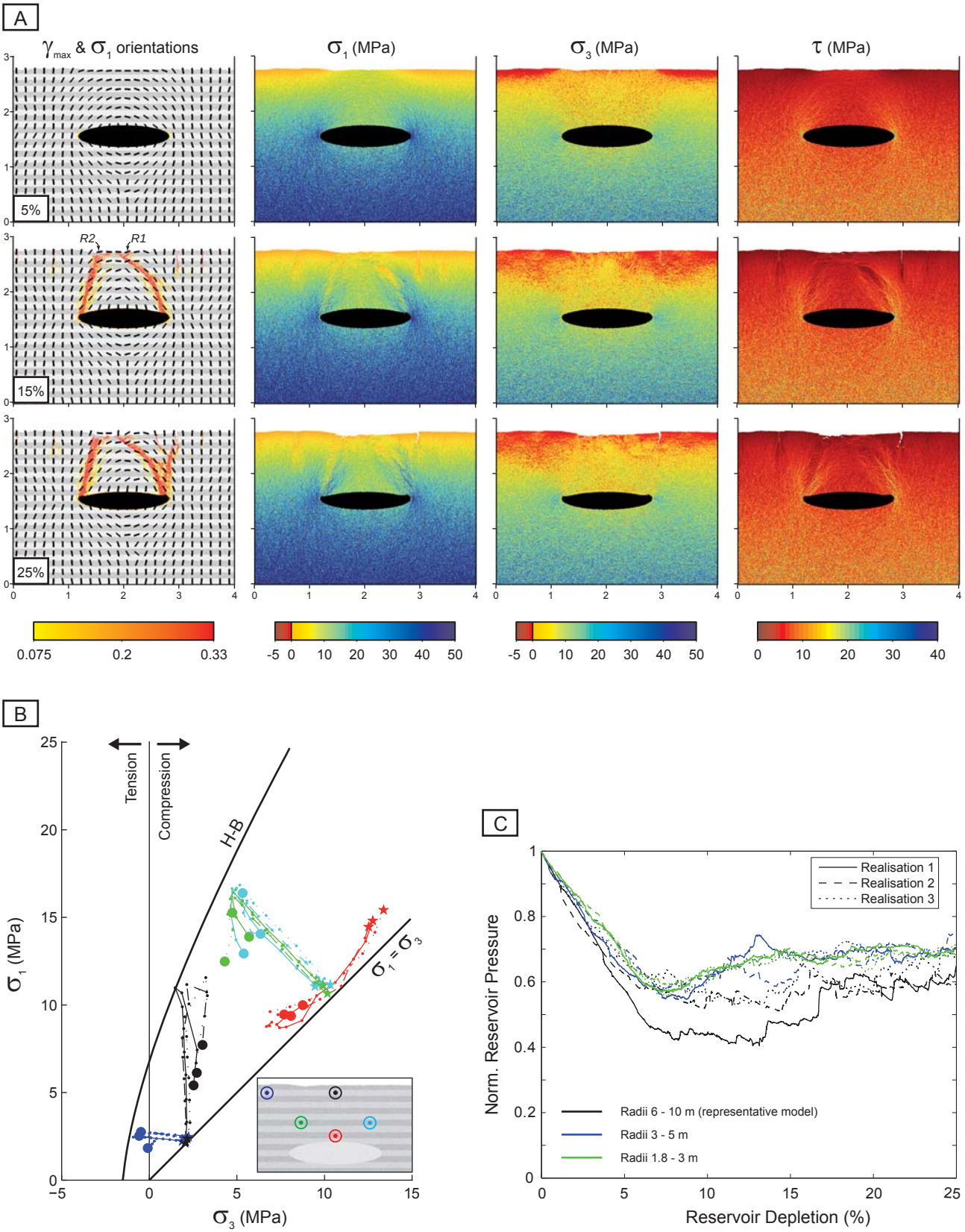

Figure S4: Effects of increasing particle resolution. **(A)** Stress and strain evolution for model with particle radii between 1.8 and 3 m. Host-rock properties are the same as in Figure 4. See caption to Figure 4 for explanation of layout and annotations. Note the fault geometry upon failure is essentially the same as in the lower resolution model in Figure 4. **(B)** Stress paths for three model realisations with particle radii between 1.8 and 3 m, run up to 10% depletion. Inset shows the initial positions of the circular areas for which each path was calculated. See caption to Figure 5 for explanation of labels and symbols. Note that stress path pattern is essentially the same as the lower resolution model in Figure 5. **(C)** Evolution of reservoir pressure (normalised to maximum) for models with increased particle resolution.

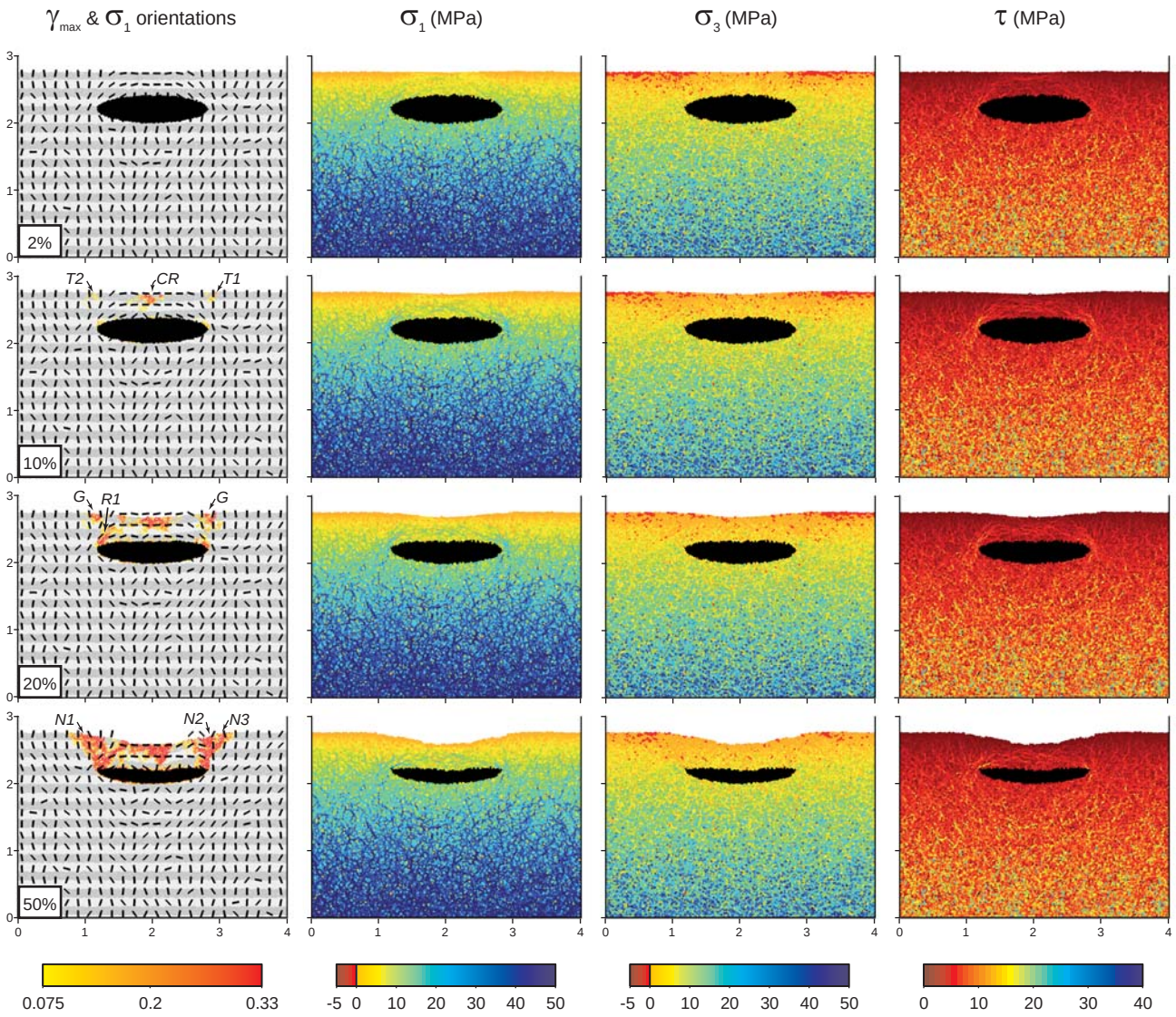

Figure S5: Stress and strain evolution during a 'central sagging' collapse style. See caption to Figure 4 for explanation of symbols and layout (except: CR, compressional ridge; G, graben). Such a collapse style emerges in low strength materials that cannot support high differential stresses (contrast with Figure S6). Nonetheless, as shown in Figure S9, the stress paths leading to failure are similar in orientation to those seen in the more typical 'single central block collapse' style (Figure 5).

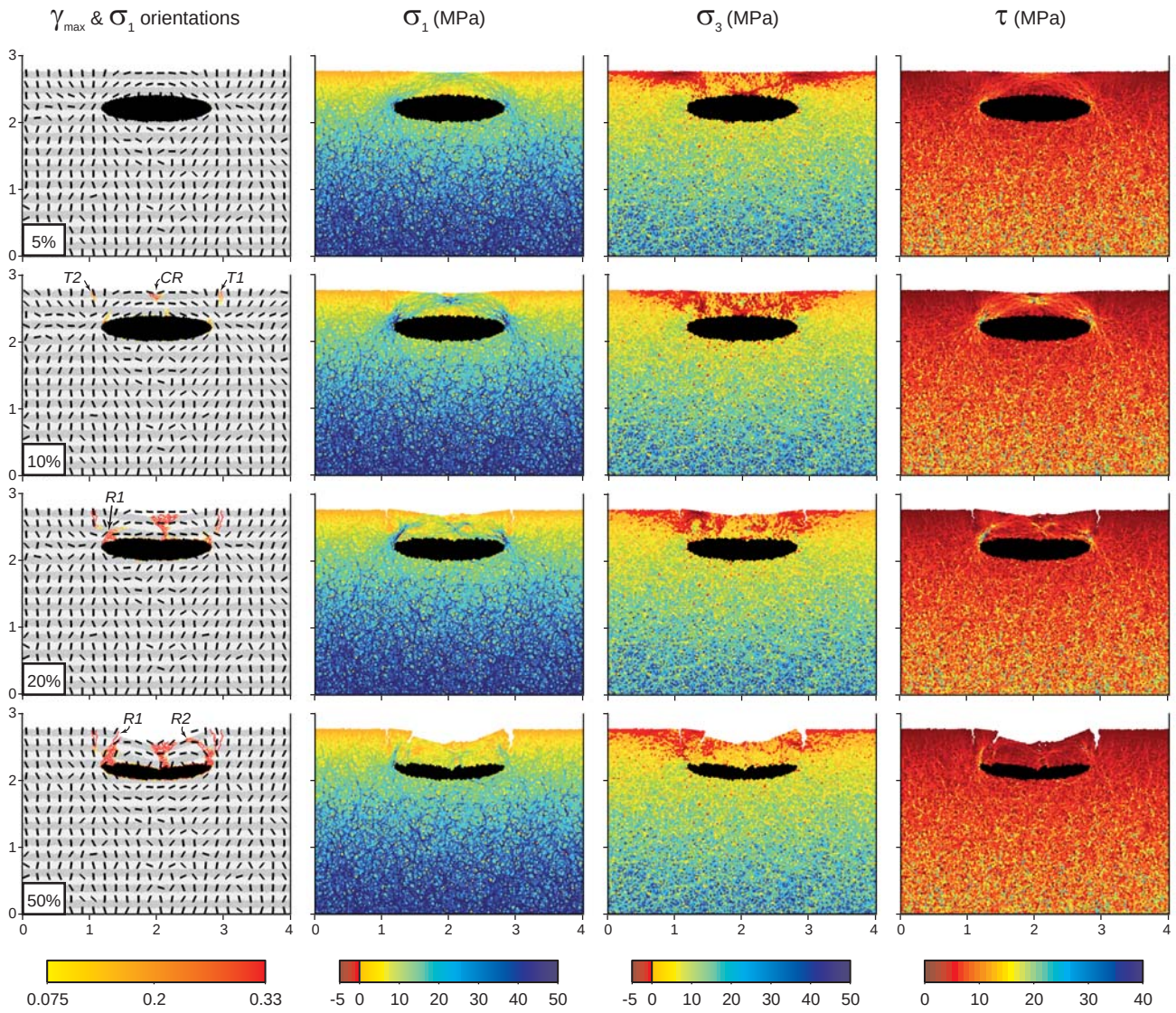

Figure S6: Stress and strain evolution during a 'central snapping' style collapse. See caption to Figure 4 for explanation of layout, symbols and labelling of fractures in the first column (except: CR, compressional ridge). Fracture labelling corresponds to that in Figures S9B and S10A. Note that the patterns of tensile and differential stress in the elastic phase (5% depletion) are very similar to that shown in Figure 1B. The predicted ultimate failure along an inward-inclined normal fault does not occur, however. Instead, and as shown in the related stress paths in Figure S9 and in the corresponding reservoir pressure vs. depletion curve in Figure S10, ultimate failure is associated with formation of a central Y-shaped fracture system ('pop-up' structure) and also of marginal outward-inclined reverse faults.

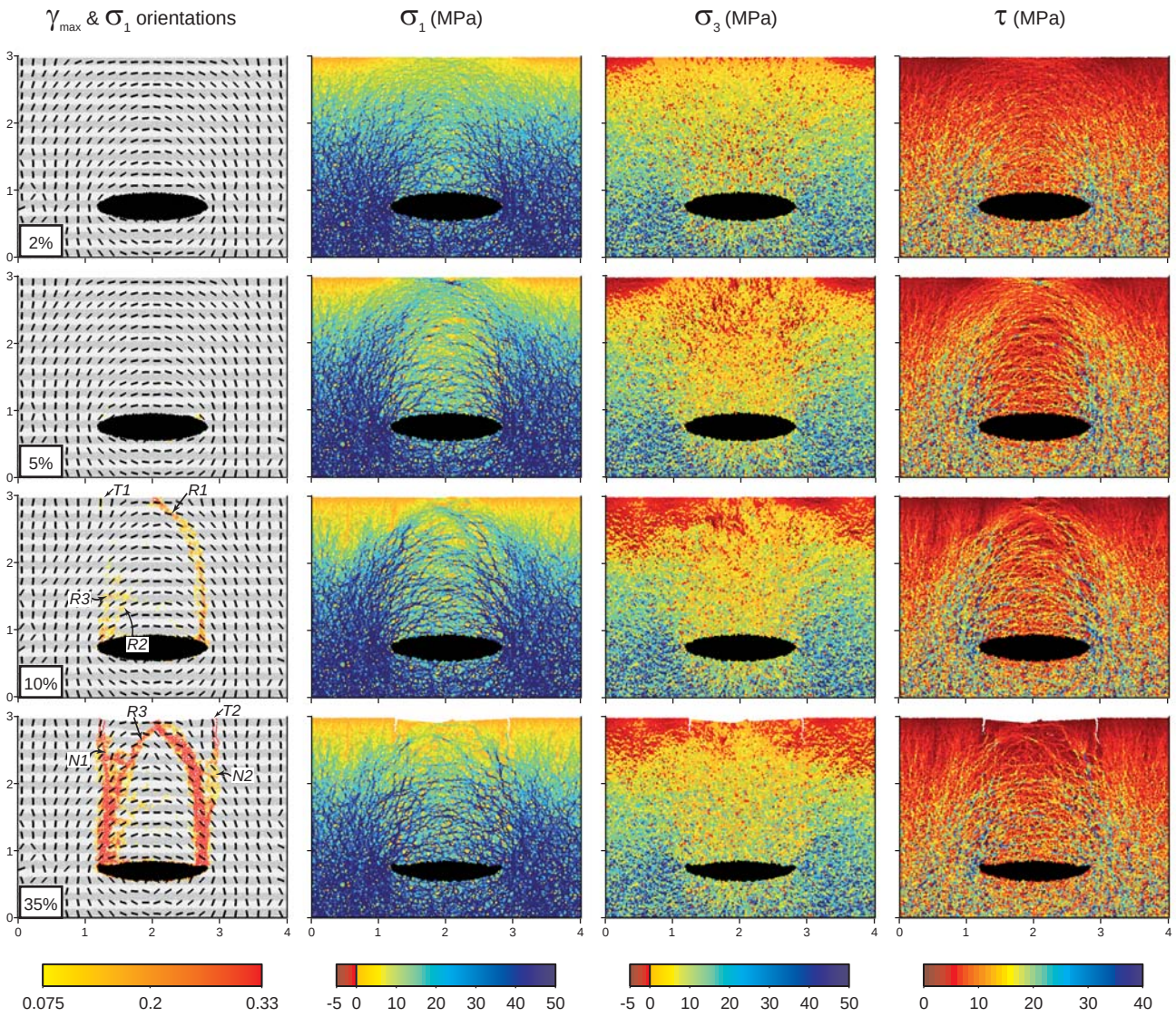

Figure S7: Stress and strain evolution in a 'single central block' collapse developing in a higher Young's modulus (10 GPa) model. See caption to Figure 4 for explanation of symbols and layout. In detail, the roof undergoes a rapid upward migration of 'damage accumulation' (i.e. bond breakage), such that the stresses seen in the elastic phase at 2% depletion are already substantially relaxed by 5% depletion (note the columnar zone of lower stresses above the reservoir). As seen in the corresponding reservoir depletion vs. pressure curve in Figure S11 (UCS = 10 MPa, T/D = 1.3), this is the 'yielding' phase in this model. Shortly afterward at c. 7% depletion, the model undergoes ultimate failure along a single through-going reverse fault, which is well expressed at 10% depletion. Accordingly, the stress paths leading to failure (Figure S9) are similar to those of the 'single central block model' shown in Figure 5.

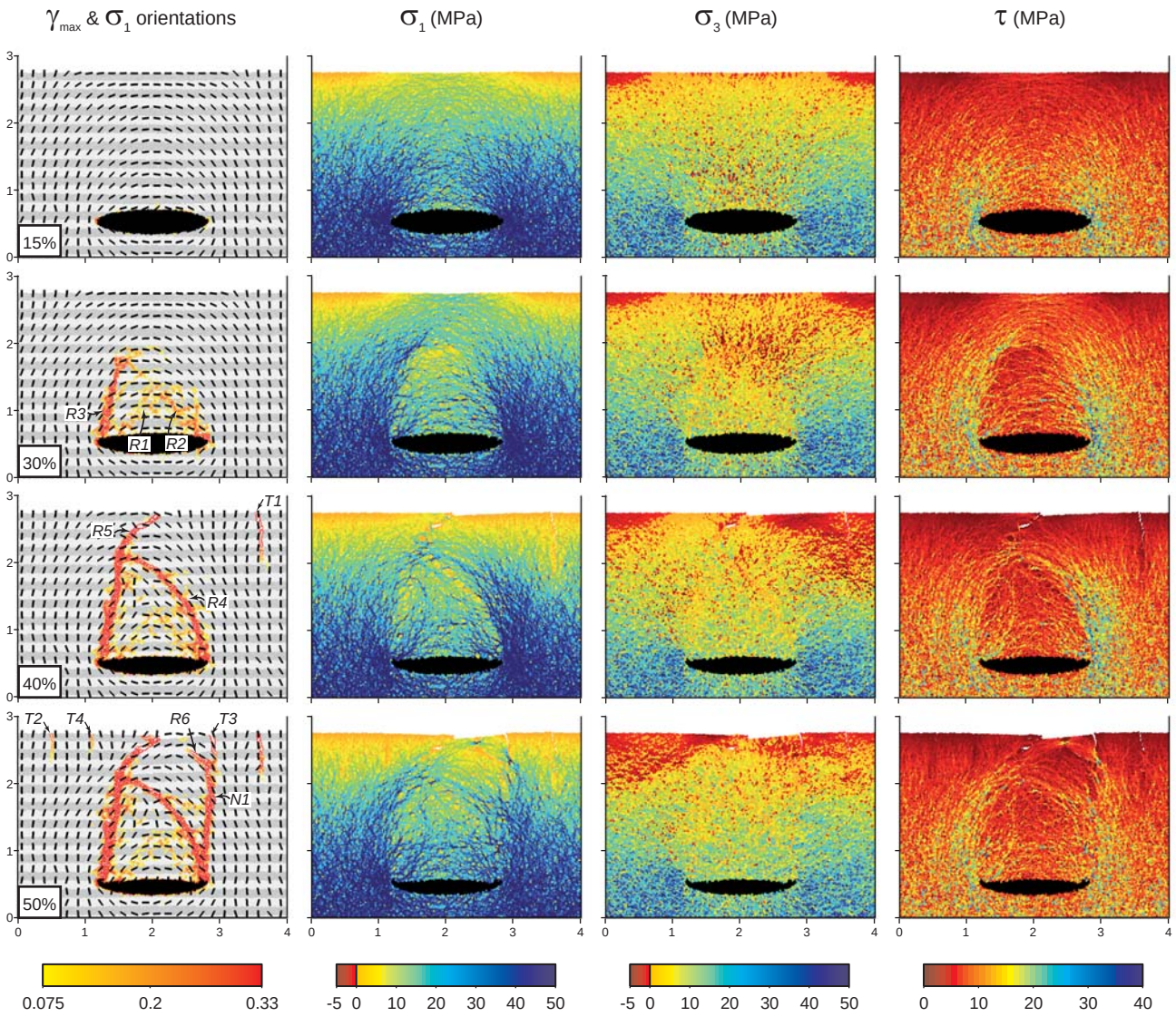

Figure S8: Stress and strain evolution during a 'multiple central blocks' collapse style. See caption to Figure 4 for explanation of symbols and layout. Fracture labelling corresponds to that in Figures S9D and S10C. In contrast to the higher modulus model in Figure S7, the accumulation of 'damage' (i.e. bond breakage) within the reservoir roof progresses more slowly upward in depletion terms. Consequently, strain localises more effectively on fractures at depth before stresses in the overlying material grow large enough to continue the upward propagation of fracturing. This leads to the clear delimitation of multiple sub-surface blocks, and gives rise to a sequential upward intensification and disruption of the stress arch (i.e. stress transfer), as the roof failure progresses from reservoir to surface.

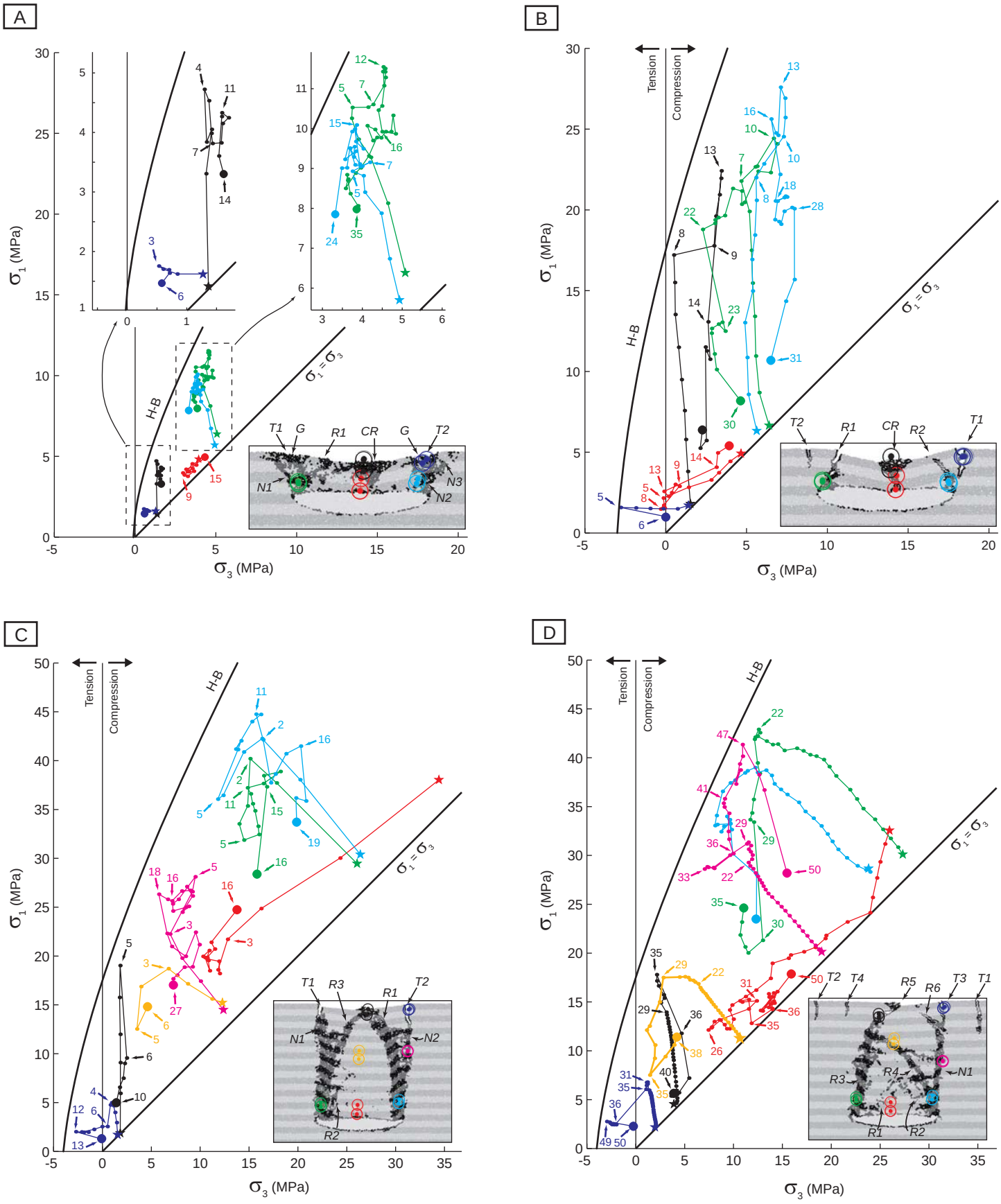

Figure S9: Principal stress paths for key roof locations during end-member caldera collapse styles (see Figure 3). **(A)** a 'central sagging' collapse; **(B)** a 'central snapping' collapse; **(C)** a 'single central block' collapse developed in a higher Young's modulus host-rock; and **(D)** a 'multiple central blocks' collapse. Paths are from the models shown in Figures S5, S6, S7 and S8, respectively. Fractures in the insets are labelled in correspondence with Figures S5-S8. See caption to Figure 5 for further description of symbols. Note that the stress path patterns in most cases are closely similar to those in the typical 'single central block' collapse style in Figure 4. The main exceptions to this is the stress paths associated with fractures R1 and R2 in the central snapping end-member. These are steeper than in other collapse styles, a fact that probably reflects the greater influence of bending stresses in this case (high strength and thin beam-like roof).

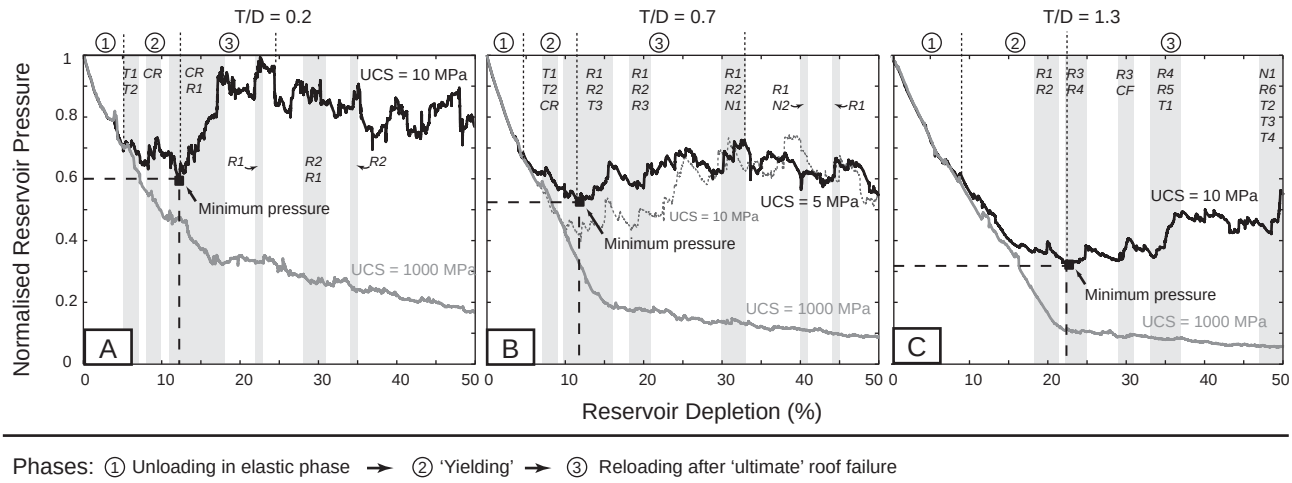

Figure S10: The influence of faulting on reservoir unloading-reloading evolution shown for selected DEM collapse models of differing roof thickness/diameter ratio. **(A)** the model in Figure S6 with UCS = 10 MPa, developing a 'central snapping' collapse style; **(B)** the model in Figure 4 with UCS = 5 MPa developing a typical 'single central block' collapse style. The grey dashed curve shows data from an equivalent model with UCS = 10 MPa; **(C)** the model in Figure S8 with UCS = 10 MPa developing a 'multiple central blocks' collapse style. The solid grey curves in each plot come from geometrically equivalent models with an 'infinitely strong' host-rock (UCS = 1000 MPa). These curves hence show a purely elastic unloading of the 'lithostatic' pressure exerted on the reservoir, plus a 'magma-static' pressure decline. The black curves also include the effects of non-elastic deformation (i.e. fracturing). The grey bars denote depletion intervals during which fractures labelled in Figures S6, Figure 4, and Figure S8, respectively, either form or undergo significant ruptures (i.e. slip events). Such fracturing effects are seen also as stress path changes in Figure 4 and in the corresponding parts of Figure S9.

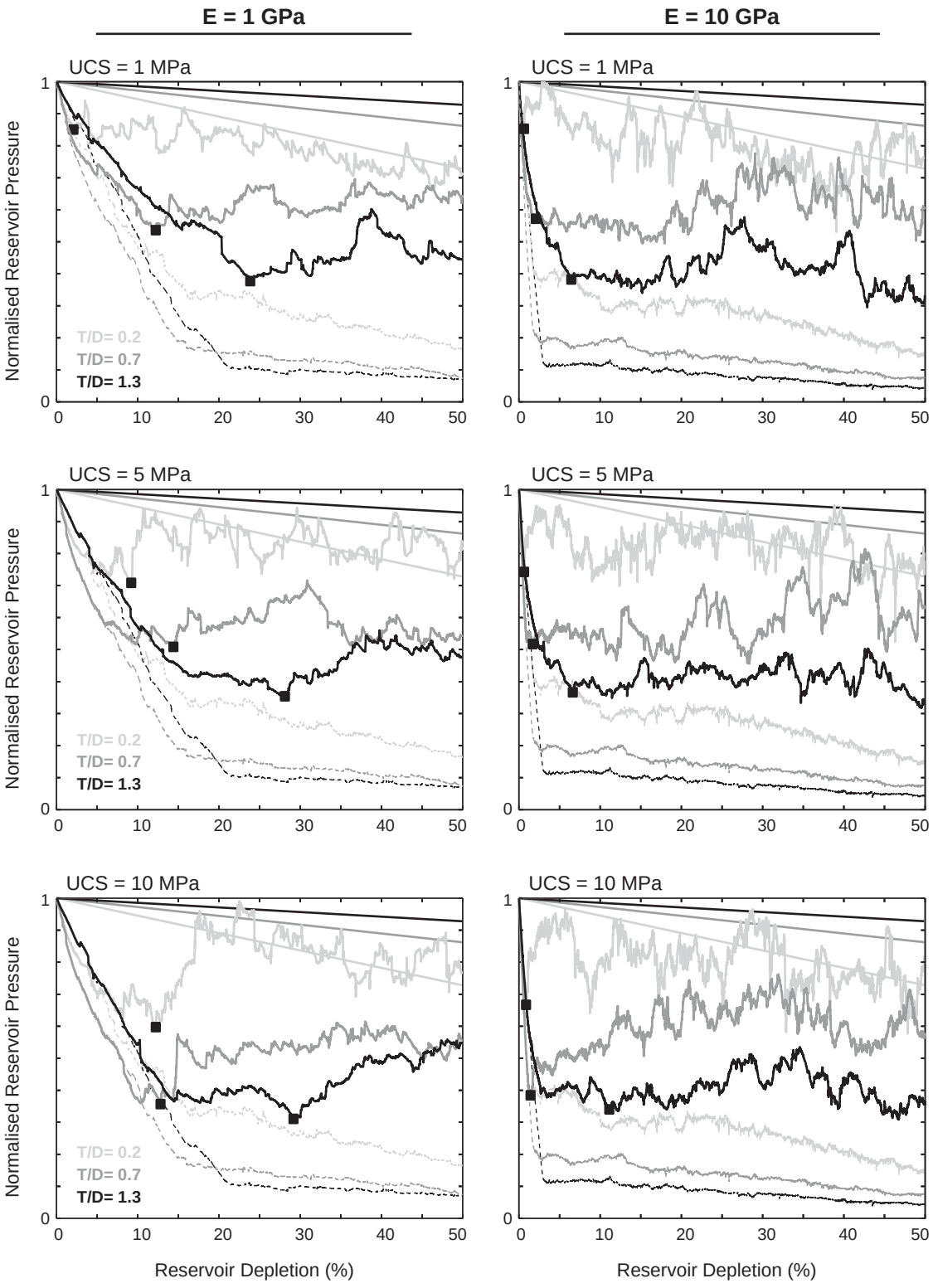

Figure S11: Reservoir unloading vs. depletion for selected caldera collapse models. The results are shown columnwise in terms of low (left) or high (right) Young's Modulus and row-wise in terms of increasing unconfined compressive strength (UCS). Each subplot shows the results of mechanically similar models with differing roof thickness/diameter ratios (T/D) and correspondingly different shades of grey. The dashed curves in each plot come from geometrically equivalent models to the correspondingly grey-shaded solid curves, but with an 'infinitely strong' host-rock (UCS = 1000 MPa). The dashed grey curves hence show a purely elastic unloading of the reservoir, plus a 'magma-static' pressure decline. In contrast, the solid grey curves also include the effects of non-elastic deformation (i.e. faulting). The comparison of dashed and solid curves helps to show the onset of yielding and failure in models with 'finite strength'. Solid sloped lines indicate the depletion-adjusted lithostatic pressure for each T/D ratio and are shaded accordingly.